Develop a LES-based air quality model by nesting DALES in LOTOS-EUROS

Jiyunting Sun

A thesis presented for the degree of Master of Sciences

Supervisors: Dr. Tim Vlemmix, Dr. Stephan de Roode

Department of Geosciences and Remote Sensing

Faculty of Civil Engineering and Geosciences

Delft University of Technology

August 2016

Abstract

Nitrogen dioxide (NO_2) is one of the nitrogen oxides (NO_x) pollutants. Not only the NO_2 itself is toxic to human health, but also the precursors of a number of hazardous secondary air pollutants, such as nitric acid, tropospheric ozone and nitrate component of particulate matters. Besides, NO_2 is also an essential substances involving in ozone destruction in the stratosphere. The main source of NO_2 over urban is combustion processes from traffic.

Jeopardized by the severe situation, the monitoring and observation to this harmful trace gas is important. For urban regions, the in-situ and remote sensing techniques are combined. However, these measurements can be problematic due to the meteorological conditions or atmospheric processes, such as clouds. Besides, the retrieval of the measurements provides limited information on concentration fields under various a-priori assumptions.

Alternatively, the atmospheric dispersion modeling is in use to study the air quality, which provides a more complete deterministic description of pollutants dispersion problem. Currently, the dominating atmospheric dispersion models are based on the parameterization. These models are efficient to simulate meso-scale or macro-scale atmospheric dispersion, with spatial resolution of magnitude of kilometers. Considering on urban scale, however, this resolution is too coarse to resolve the air pollutants, where the emission sources are close to receptors. Instead, a more effective technique is large eddy simulation (LES). It applies a low-pass filter that effective removes small-scale turbulences from numerical calculation. By nesting DALES (Dutch Atmospheric Large Eddy Simulation) into LOTOS-EUROS (LOng Term Ozone Simulation-EURopean Operational Smog model), an air quality module is developed to evaluate the LES-based air quality model by comparing with LOTOS-EUROS.

The conclusion of this thesis consists of two parts. The first one is the sensitivity study, where the properties of DALES original chemical module are explored. These properties includes the sensitivity of NO_2 concentration to background ozone level, reaction rate coefficient, clouds perturbation and turbulent control. In the second part, simulation over Rotterdam is operated on a relative coarse resolution, as the consequence of the limitation of restore space and process capability. The slab averaged profiles are not significantly different because of the strongly constrained concentration boundary condition by LOTOS-EUROS. Although attempt to study the difference of concentration field due to the dynamics scheme is not achieved, DALES still has much higher resolution compared with LOTOS-EUROS. Hence, the spatial variability in DALES is more detailed. Conclusively, the DALES air quality module performs consistently with LOTOS-EUROS. The improvement in terms of chemical mechanism, the emission inventory, the capability of processing. etc. will complete this module in future.

Acknowledgement

This master thesis is my final project of my Geoscience and Remote Sensing study at Delft University of Technology, which combines my knowledge of atmosphere physics and atmospheric compounds remote sensing acquired during the two year master program. It takes the first step to develop an add-on module based on a large eddy simulation model, and serves as the reference material for researchers who are interested in atmospheric dispersion or trace gases retrieval from remote sensing measurements.

I would like to take the opportunity to thank some people that helps me a lot. First of all, I would like to thank Dr. Tim Vlemmix. As the main supervisor, he created the chance to let me work with atmospheric numerical modeling. He also provided the detailed guidance and support throughout the project. Then, I would like to thank Dr. Stephan de Roode for his guidance on knowledge of atmospheric physics and operation of Dutch Atmospheric Large Eddy Simulation (DALES). Furthermore, I would like to thank technical support Erwin de Beus, who offered me the facility to exert the experiments and helped me to solve technical problems with great patience. Finally, I would like to thank Martijn Schaap, Sjoerd van Ratingen and Richard Kranenburg from TNO, who offer the simulation outputs of LOTOS-EUROS and URBIS traffic emission inventory. Additionally, a spacial thank goes to Pim van Dorp, who shared his experience in DALES with me.

Working with this project is a challenging experience. It consolidates my understanding in trance gases retrieval on the one side, and provides the valuable opportunity to work in detail with numerical model on the other side. I would like to thank all the people that accompanied with me to finish this project.

Contents

Chapter 1

Introduction

Since industrialization onset, the anthropogenic air pollution over urban area has expanded dramatically, mainly due to the growing use of fossil energy to meet the economic demands. The influence of air pollution could be comprehensive. On the one hand, human health can be directly threatened by the pulmonary deposition and absorption of inhaled chemicals; or, the air pollutant deposits into natural receptors and enters into food chain, causing additional sources of human exposure. On the other hand, the ecosystem is also a victim of air pollution by disturbing the balance of structure and function of ecosystem [WHO et al.(2000)]. During the last few decades, ambient air quality has improved among most of European countries. But even under the common levels achieved at present, exposure to air pollution still has substantial adverse effect on human health [WHO et al.(2003)]. The World Health Organization (WHO) report in 2014 [WHO et al.(2014)] reveals that even in high-income countries of Europe, deaths caused by ambient air pollution in year 2012 was up to 280,000, which was the highest among all developed areas in worldwide.

Jeopardized by the severe situation, a better understanding of the mechanism of chemical composition in the atmosphere is urgently required. The air pollutants could be near around where they are released, or disperse over larger distance from emission sources. Consequently, the local and regional, or even global properties of air pollution is necessary to be observed, which can be realized by combination of in-situ and remote sensing techniques. These measurements give quantitative information about ambient concentration and deposition of chemical compounds. But they could be easily limited by meteorological conditions or atmospheric processes . In extreme case, for example, the satellite measurement is almost blind to surface concentration of target air pollutants if there exist optically dense clouds. Under this condition, the retrieved vertical column density (N^V, Appendix. C.18) is not necessarily equal to the value in reality. Even under clear sky, the space-borne techniques still fail to retrieve the vertical profile ($c(z)$) so far, which means the concentration at surface level ($c(0)$) that mostly affects public health, is unknown (Equation. 1.1, where z is the height, and $s(z)$ is the ratio between upper level to surface level concentration, which describes the shape function). Besides, air mass factor (AMF, Appendix. C.19), which is the key parameter to convert measured slant column density (N^S, Appendix. C.17) to N^V, also depends on the

trace gases and aerosols profile shape.

$$N^V = \int_0^{TOA} c(z)dz = c(0)\int_0^z s(z)dz \tag{1.1a}$$

$$s(z) = \frac{c(z)}{c(0)} \tag{1.1b}$$

Therefore, another important technique is essential to study the mechanism of air pollutants, which is atmospheric numerical modeling. Unlike measured data, this numerical tool provides a more complete deterministic description of air quality problem, and is the only method quantifying the deterministic relationship between emissions and concentrations, including the consequences of past and future scenarios and assessment of the abatement strategies [Daly and Zannetti(2007)]. In other words, the simulated results are capable to provide the full information of vertical profile and surface concentration ($c(0)$). Currently, majority of air quality models applied to the Netherlands are based on either Eulerian dispersion model, e.g. LOTOS-EUROS (LOng Term Ozone Simulation - EURopean Operational Smog model, [Schaap et al.(2005a)]) with resolution of 7 $km\times$ 7 km, or Lagrangian dispersion models like OPS (Operational Priority Substances Model, [van Jaarsveld et al.(2015)]), where liner method is used for chemical reaction, except for the reaction of acidifying substances, conversion and deposition that are based on non-linear reaction. Gaussian dispersion model is not common nowadays due to over simplified parameterization, representative model is STACKS (Short-Term Air pollutant Concentrations, Kema modeling System, [Erbrink(1995)]).

All model types mentioned are efficient to simulate meso-scale or macro-scale atmospheric dispersion, with spatial resolution of magnitude of kilometers. Whereas, if considering urban air pollution, where emission sources and receptors may distance is within few hundred meters, all these models become too coarse to resolve the air pollutant dispersion on such a spatial scale. Instead, new approaches are proposed, in order to combine high horizontal resolution with a realistic vertical dimension. Driven by the development of computation capability, the dispersion due to turbulence is no longer only solved by parameterization, instead, a state-of-art technique, large eddy simulation (LES), becomes popular in solving planetary boundary layer problems. At present, however, it is a pity that there is no independent air quality model developed that is LES-based in the Netherlands.

This master thesis, therefore, takes the first step to develop of a LES-based air quality model by nesting DALES (Dutch Atmospheric Large-Eddy Simulation, [Heus et al.(2009)]) into LOTOS-EUROS. To study the concentration fields of classic pollutants in cities, namely nitrogen oxides (NO_x) and ozone (O_3). The research is settled on local and regional scale over the Rotterdam region. This model is, in future, expected to serve several objectives: to investigate the relation between N^V and $c(0)$ (and its dependency to spatial scales), to explore what agreement to expect between ground-based and satellite column measurements in the same region with scattered sources, and to simulate the optimal profile shape needed to calculate the AMF that itself is required to convert N^S to N^V.

This thesis introduces the urban air pollutants and the comprehensive overview of air quality models in Chapter 1, followed by Chapter 2 consisting of the detail introduction of DALES model setting and the main techniques applied to this thesis. The first part of Chapter 3 contains a series of sensitivity study of NO_2 concentration field to dynamics and chemistry. The remaining is the simulation over Rotterdam region, with vertical, horizontal and temporal comparison with LOTOS-EUROS. Lastly, the main conclusions and outlooks are listed in Chapter 4.

1.1 Classic urban chemical species

1.1.1 Nitrogen oxides

Nitrogen oxides (NO_x), mainly including nitric oxide (NO) and nitrogen dioxide (NO_2), are emitted from lightning, natural fires and soils, and combustion of fossil fuels and biomass [Beirle(2004)]. The anthropogenic process nowadays contributes to the major part of the NO_x emission, particularly in urban outdoor areas. Though NO_x also covers oxides of nitrogen species, in this thesis the NO_x refers to NO and NO_2 only, and the main focus would be on NO_2, since the NO converts to NO_2 too rapidly to be detected in observation.

The environmental effect of NO_2 is complicated. It not only a precursor for a number of hazardous secondary air pollutants, e.g. nitric acid and nitrate component of particulate matters (PM). Such nitrogen-containing air pollutants could endanger the ecosystem, presented as, for example, soil acidification, which further damages vegetation growth by increased soil solution of aluminum concentration, or surface waters acidification and fish mortality, etc [WHO et al.(2003)]. Also, NO_2 is one of the most essential substances participating in ozone (O_3) destruction in the stratosphere, which is a key to the balance of the global radiative budget and oxidizing capacity of the atmosphere [Beirle(2004)].

On the another hand, NO_2 poses a threat on human health by attacking the respiratory tract. Experiments show that asthmatics appear to be more susceptible to acute exposures. Compared with normal healthy people, who are generally do not affected by NO_2 concentration lower than 1 ppm, while the mild asthmatics are influenced by the lowest concentration 0.3 ppm for lasting 30 to 110 minutes exposure. The increased respiratory symptoms, their duration, and lung function decrements are qualitatively associated in children with long-term ambient NO_2 exposure [WHO et al.(2003)].

Not only NO_x themselves, they are also considered to be precursors of tropospheric ozone (O_3), which is also a pollutant with adverse effect to health. As reported, ozone at background levels is mainly from anthropogenic origin, ranging from 0.02 to 0.035 ppm, while for short exposure the value can be doubled. In Europe, maximum hourly ozone concentration can exceed 0.18 ppm in urbanized regions [WHO et al.(2000)].

1.1.2 Overview of chemistry of nitrogen oxides, ozone and VOCs

The tropospheric ozone (O_3) is important to photochemically form the excited oxygen atom $O(^1D)$ (Reaction. 1.2), which is further deactivated to ground-state oxygen atom $O(^3P)$ (Reaction. 1.3), or reacts with water vapor to from hydroxyl radicals OH (Reaction. 1.4),

$$O_3 + h\nu \rightarrow O_2 + O(^1D) \tag{1.2}$$

$$O(^1D) + M \rightarrow O(^3P) + M \qquad (M = N_2, O_2) \tag{1.3a}$$

$$O(^3P) + O_2 + M \rightarrow O_3 + M \qquad (M = N_2, O_2) \tag{1.3b}$$

$$O(^1D) + H_2O \rightarrow 2OH \tag{1.4}$$

, Reaction.1.3 is therefore balances the loss of O_3 by photolysis (Reaction. 1.2), while Reaction. 1.4 leads to net loss of tropospheric O_3. In the cycle of NO_x, the O_3 is also balanced (Figure .1.1 Scheme A). Starting with the emission of NO, it rapidly reacts with O_3 to form NO_2. Then tropospheric O_3 is formed photochemically from NO_2,

$$NO + O_3 \rightarrow NO_2 + O_2 \tag{1.5a}$$
$$NO_2 + h\nu \rightarrow NO + O(^3P) \tag{1.5b}$$
$$O(^3P) + O_2 + M \rightarrow O_3 + M \qquad (M = N_2, O_2) \tag{1.5c}$$

However, this equilibrium would be disturbed by the presence of volatile organic compounds (VOCs). VOCs are generally categorized as either methane (CH_4) or non-methane (NMVOCs), including isoprene (C_5H_8), formaldehyde (CH_2O), etc. VOCs are emitted from natural (natural wetlands, vegetation, etc) and anthropogenic sources (domestic ruminants, rice paddies, combustion of biomass, fossil fuels, fuel storage and transport, solvent usage, emissions from industrial operations, landfills, and hazardous waste facilities, etc.). The overall chemical scheme of nitrogen oxides, ozone and VOCs is shown in Figure. 1.1 Scheme B. The degradation reactions of VOCs forms intermediate $\dot{R}O_2$ andHO_2 radicals, which directly convert NO to NO_2 (Reaction. 1.6),

$$HO_2 + NO \rightarrow HO + NO_2 \tag{1.6a}$$
$$R\dot{O}_2 + NO \rightarrow R\dot{O} + NO_2 \tag{1.6b}$$

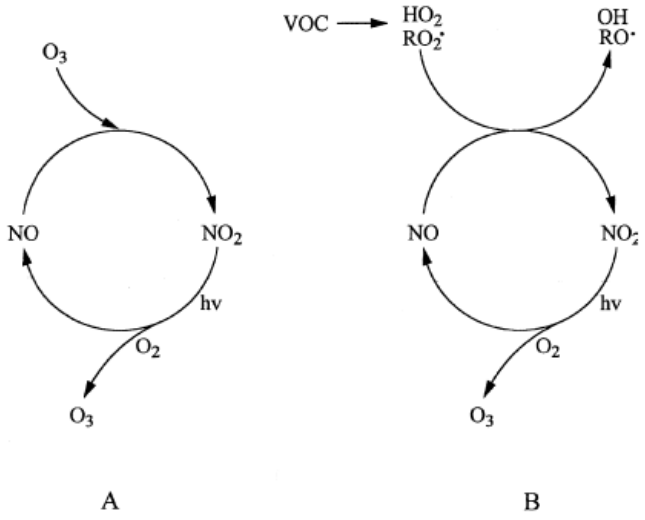

Figure 1.1: Chemical schemes. (A) absence of VOCs: the NO_x and O_3 are in balance; and (B) presence of VOCs: net formation or loss of O_3, depending on the concentration of NO and reaction rate with HO_2 and RO_2. (Figure source: [Atkinson(2000)])

, and further forms tropospheric O_3 (Reaction. 1.5b and 1.3b). If the NO concentration is relatively low, O_3 will react with OH and HO_2, leading to additional loss of tropospheric O_3,

$$OH + O_3 \rightarrow HO_2 + O_2 \tag{1.7a}$$

$$HO_2 + O_3 \rightarrow HO + 2O_2 \tag{1.7b}$$

Therefore the net formation of O_3 (Reaction 1.5b) and net consumption of O_3 in the troposphere depends on the NO concentration. This is determined by the reaction rate coefficients between NO and intermediate $\dot{R}O_2$ andHO_2 radicals.

Overall, the chemical scheme for the system of NO_x falls into two cases. One is without VOCs; the other is $NO_x - O_3 - VOCs$ chemical scheme, where the balance between O_3 production and consumption depends on NO concentration, with respect to reaction rate coefficients of HO_2 and $R\dot{O}_2$, and concentration of HO_2 and NO [Logan(1985)]. This thesis aims to evaluate the difference brought by dynamics, hence, only the case without VOCs is applied to the academic experiments and simulation over Rotterdam area.

1.2 Overview of air pollutants dispersion modeling

Atmospheric dispersion modeling mathematically describes how air pollutants are transported in the ambient atmosphere. This process is dominated by advection field, together with influences from turbulence, chemical reaction and removal of deposition. Among these dominant factors, turbulence is the key determining the accuracy and precision of a numerical model, because it is highly chaotic. In this thesis, the criteria to classify the air quality models lies in how the model treats turbulences.

The dispersion of air pollutants in differential form equation is as shown in Equation.1.8, where i is the index of species, D_i is the molecular diffusion coefficient, the source term S_i contains deposition, R_i is the net production (or depletion if negative) by chemical reaction [Garg(1998)],

$$\frac{\partial c_i}{\partial t} = -\nabla(c_i\vec{u}) + \nabla^2(D_i\nabla c) + S_i + R_i \tag{1.8}$$

The turbulent influence is involved by applying Reynold's averaging theory (Equation.1.9), with divides wind and concentration field into time averaged and turbulent perturbation, with assumption that the time averaging of turbulent perturbation is zero,

$$\vec{u} = \overline{\vec{u}} + \vec{u}' \tag{1.9a}$$

$$c_i = \overline{c_i} + c_i' \tag{1.9b}$$

$$\frac{\partial \bar{c}_i}{\partial t} = -\nabla(\overline{\vec{u}}\overline{c_i}) - \overline{\nabla(\vec{u}'c_i')} + \nabla^2(D_i\nabla\bar{c}_i) + S_i + R_i \tag{1.9c}$$

The remaining turbulence term $\overline{\nabla(\vec{u}'c_i')}$ is a closure problem that infinite variables and equations need to solve the definite $\frac{\partial \bar{c}_i}{\partial t}$. Normally, to solve turbulent dispersion, either using analytical or numerical methods. The numerical method applies parameterization to express the turbulence fluxes, or by direct dynamic simulation that constructs turbulent equations, or combined solutions.

1.2.1 Analytical solution: Gaussian dispersion model

Gaussian dispersion model is one of the classic analytical solution to Equation.1.9c. Under circumstance of a homogeneous, steady-state flow and a steady-state point source, the air pollutant dispersion equation mention above can be integrated analytically (Equation.1.10):

$$c(x,y,z) = \frac{Q}{2\pi\sigma_y\sigma_z u} exp\left(\frac{-y^2}{2\sigma_y^2}\right)\left(exp\left(\frac{-(z-h)^2}{2\sigma_z^2}\right) + exp\left(\frac{-(z+h)^2}{2\sigma_z^2}\right)\right) \tag{1.10}$$

, where c is the concentration at specific location; Q represents the point source; x, y and z are downwind, crosswind and vertical direction, respectively; σ_y and σ_z are crosswind and vertical standard deviation of emission distribution, which are derived from horizontal and

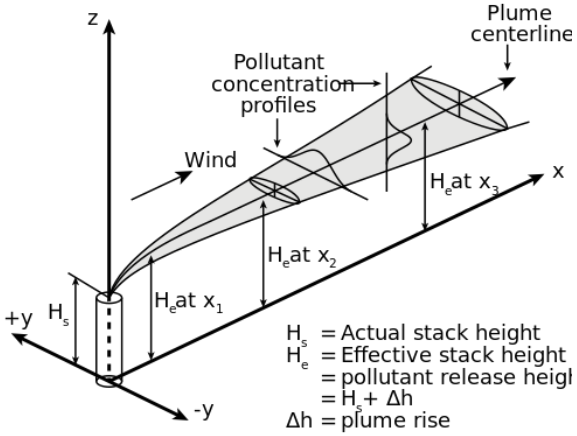

Figure 1.2: Gaussian dispersion model. The effective stack height should includes actual stack height and effective stack height. (Figure source: wikipedia).

vertical diffusion coefficient K_h and K_z, respectively. This will be explained in the following section; u is the wind speed; h is the emission released height.

This kind of model does not consider dry and wet deposition, also the gravitational settling and chemical reactions. Besides, Gaussian dispersion model assumes advection overwhelming diffusion term, which could lead to large error under circumstance when wind speed is relatively low. The release height h, which is assumed to be at top of stack (Figure.1.2), where there is maximum concentration. But in case of buoyant plume, the effective stack height is of necessity to be estimated because of the plume rise. Thus, an improved Gaussian dispersion model includes such correction for the plume height.

1.2.2 Numerical parameterization:K-theory based models

As shown in Equation.1.9c, the turbulence diffusion term $\overline{\nabla(\vec{u'}c_i')}$ is a challenge due to closure problem. The simplest first-order solution for turbulence parameterization by gradient transport theory, the so-called K-theory. That is, the $x-$ directional turbulence is proportional to the gradient of concentration field of chemical species i (Equation.1.11). This method limits models that can be only efficient at meso-scaler or macro-scale. At present, majority of Lagrangian and Eulerian dispersion models apply K-theory to parameterize turbulence.

$$\overline{u'c_i'} = -K_x \frac{\partial \overline{c_i}}{\partial x} \tag{1.11}$$

1.2.2.1 Lagrangian dispersion model

In Lagrangian dispersion model, the pollutant particles transport along the trajectories that determined by wind, turbulence and buoyancy, etc. The concentration is either estimated by numerous particles distribution in the domain, i.e. trajectory model, or by superposition of numerous Gaussian distributions with assumption that for every single unit of pollutant follows Gaussian dispersion model, i.e. puff model.

Trajectory model solves ordinary differential equation (ODEs) based on stochastic simulation for numerous of pollutant particles. The trajectory for a single particle is,

$$\frac{d\vec{r}}{dt} = \vec{v} + \vec{v_t} \tag{1.12}$$

, where $\vec{r}$ is the position of a particle, $\vec{v}$ is the dispersion speed affected by advection, gravitational setting and buoyancy, $\vec{v_t}$ is the speed influenced by turbulent fluctuation. The last term can be described as random walk in a viscous fluid by Langevin equation. Taking vertical direction for example,

$$dw_t = -\frac{w_t}{T_l}dt + \sqrt{\frac{2\sigma_w^2}{T_l}}dW \tag{1.13}$$

, where T_l is a Lagrangian timescale, σ_w represents the vertical turbulent fluctuation, dW is the white noise process with mean zero and variance dt. The first term represents autocorrelation while the last term is a random walk. When T_l is large, the autocorrelation term is relatively small, the turbulence diffusion can be regarded as an uncorrelated random walk. Therefore, for long distance simulation, the trajectory mode leads to more reasonable results.

The Equation. 1.12 assumes Gaussian turbulence, which only can be applied to isotropic turbulence and neutral condition. For anisotropic turbulence, the separated Langevin equations for each component with different turbulent fluctuations and Lagrangian timescales are applied. It has been proved to be reasonable for meso-scale and macros-scale without considering cross-correlations of turbulent fluctuations.

Puff model is developed from Gaussian dispersion model. It divides pollutant mass into units, and assume in each unit the concentration follows Gaussian distribution. The difference between the two model is the central line of plume in Puff model is no longer straight along downwind direction, instead is the Lagrangian trajectory. The concentration field is the superposition of each unit,

$$c(x,y,z) = \frac{Q\Delta t}{(2\pi)^{\frac{3}{2}}}\sum_{k=1}^{N}\frac{1}{\sigma_{xk}\sigma_{yk}\sigma_{zk}}exp\bigg(-\frac{(x_k-x)^2}{2\sigma_{xk}^2}-\frac{(y_k-y)^2}{2\sigma_{yk}^2}-\frac{(z_k-z)^2}{2\sigma_{zk}^2}\bigg) \tag{1.14}$$

, where $Q\Delta t$ is the time dependent source term; N is the number of divided units; x_k, y_k and z_k represent the location of kth unit; σ_{xk}, σ_{yk} and σ_{zk} are directional standard deviation of the Gaussian distribution for kth unit. The turbulence in Puff model can be calculated with a stochastic random walk in the trajectories, or by the deviation of the inside Gaussian distribution.

1.2.2.2 Eulerian dispersion model

Instead of a moving framework used in the Lagrangian model, Eulerian dispersion model applies fixed three-dimensional Cartesian gird as reference frame. The approach to calculate the turbulence is based on gradient transport theory as mentioned before. This will be further discussed in Section 1.3 together with introduction of LOTOS-EUROS transport scheme.

1.2.3 Numerical simulation: direct numerical simulation

The improvement of computation capability has led to the development of Computation Fluid Dynamics (CFD) technology. It enables to define the governing equations requirements of each user. This flexibility makes CFD widely used in micro-scale dispersion modeling. In contrast to previous types of models, CFD-based model solves partial differential equations (PDEs) numerically. A common technique to solve these PDEs is the Method of Lines. Firstly, spatial discretization is applied to Equation. 1.15a by grid mesh. Consequently, the original PDEs are decomposed into a system of ODEs that only depends on time; then, the ODEs are solved as initial value problem and temporally integrated.

A representative model, Direct Numerical Simulation (DNS) is the most precise among current models, because it fully simulates turbulence with a wide range of time and length scales, without any turbulent model. All the spatial scales must be resolved in mesh. However, the computational cost is extremely high, thus is only applicable to micro-scales.

1.2.4 Numerical simulation: large eddy simulation

For a simulation at urban-scale, both K-theory based models and DNS become problematic. The trade-off between higher spatial resolution and less computational cost leads to solution of Large Eddy Simulation (LES). As an alternative to DNS that solves PDEs numerically, LES reduces computational cost by a low-pass filter that effectively removes small-scale turbulences from numerical calculation. Hereafter, these filtered turbulences are further parameterized by models for unresolved scales. The result therefore consists of filtered transport equations (Equation. 1.15a) and a residual term (Equation. 1.15b) [Burton(2005)],

$$\frac{\partial \widetilde{c_i}}{\partial t} = -\nabla(\widetilde{\vec{u}}\widetilde{c_i}) + \nabla^2(D_i \nabla \widetilde{c_i}) + S_i + R_i + \nabla \vec{\sigma_i} \tag{1.15a}$$

$$\vec{\sigma_i} \equiv \widetilde{\vec{u}c_i} - \widetilde{\vec{u}}\widetilde{c_i} \tag{1.15b}$$

, where the $\widetilde{(\cdot)}$ means averaged within filter width; i is the index of chemical species; D_i is the molecular diffusion coefficient; S_i and R_i present the source and net production (or depletion if negative) by chemical reaction, respectively; the last term in Equation.1.15a is the SFS model (Equation.1.15b). The unresolved turbulence scales fall into two categories, sub-filter scale (SFS) and sub-grid scale (SGS). SFS contains scales with wave numbers larger than cutoff number of filter but the effects are dampened, these scales must be reconstructed. While SGS is the scale smaller than filter width. But in practice, LES applies filter width as a function of LES grid size, typically from 1 m for stable stratification boundary layers, to 50 m for cloud-topped atmospheric boundary layer [Heus et al.(2010)].

1.3 Eulerian dispersion model: LOTOS-EUROS

LOTOS-EUROS is a Eulerian chemical transport model by integrating of two operational models, i.e. LOTOS ((LOng Term Ozone Simulation) and EUROS (EURopean Operational Smog model), which were independently developed by Netherlands Organization for Applied Scientific Research (TNO) and National Institute for Public Health and the Environment (RIVM), respectively. Thus, there is no surprise that two models differ in technical structure [Schaap et al.(2008)]. Besides, the projection and input meteorological data also distinguish LOTOS from EUROS. However, both models have common in master domain, chemistry, emission, land uses, and wet and dry deposition [Schaap et al.(2008)]. Based on these facts, the long-term cooperation between TNO and RIVM/MNP was established, leading to formation of LOTOS-EUROS.

1.3.1 Domain

In LOTOS-EUROS, the horizontal domain covers from 35°N to 70°N and 10°W to 60°E, and the standard grid resolution is 0.50° longitude and 0.25° latitude (25 km×25 km). Vertical height is divided into one optional surface layer with fixed depth of 25 m, and three dynamic layers consisting of one mixing layer and two reservoir layers up to 3.5 km. The mixing layer height is determined by either interpolated meteorological observation or ECMWF (European Centre for Medium-Range Weather Forecasts) analysis [Schaap et al.(2005b)].

1.3.2 Inputs

Meteorological field of LOTOS-EUROS is input every 3 hour, deriving from either observations of the Free University of Berlin or ECMWF. The parameters include temperature, humidity, density, wind direction and speed, mixing layer height, precipitation rates, cloud cover, boundary layer and surface variables [Schaap et al.(2008)].

Both anthropogenic and biogenic emissions are involved in this model. The former consists of TNO-MACC(III) emission inventory and CAFE (Corporate Average Fuel Economy) baseline emission for 2000, while latter is calculated by meteorological data.

Land uses data for majority of Europe come from PELINDA. The principle to classify the land uses is NOAA A VHRR NDVI maximum value composites.

1.3.3 The transport equation

The main prognostic equation embedded In LOTOS-EUROS is the continuity equation (Equation. 1.16) describing the concentration variation in time due to transport, diffusion, chemistry, deposition, emission and entrainment (detrainment):

$$\frac{\partial C}{\partial t}+U\frac{\partial C}{\partial x}+V\frac{\partial C}{\partial y}+W\frac{\partial C}{\partial z}=\frac{\partial}{\partial x}\left(K_h\frac{\partial C}{\partial x}\right)+\frac{\partial}{\partial y}\left(K_h\frac{\partial C}{\partial y}\right)+\frac{\partial}{\partial z}\left(K_v\frac{\partial C}{\partial z}\right)+E+R+Q-D-W \tag{1.16}$$

, C is the concentration of chemical composition that to be calculated; U, V and W are the large scale wind components in west-east, south-north and vertical direction. The horizontal advection terms U and V are determined by meteorological fields, with considering orographic influence on wind. In the vertical direction, W is computed by model from the convergence and divergence model; K_h and K_v represent the horizontal (Equation. 1.17a) and vertical (Equation. 1.17b) diffusion coefficient, respectively,

$$K_h = \eta \sqrt{\left[\left(\frac{\partial V}{\partial x}\right)^2 + \left(\frac{\partial U}{\partial y}\right)^2\right]} \tag{1.17a}$$

$$K_v = \frac{\kappa U_*}{\phi\left(\frac{z}{L}\right)} \tag{1.17b}$$

, where κ is the Karman constant, U_* is the friction velocity (Appendix. C.10), z is the height, L is the Monin-Obukhov length (Appendix. C.11), ϕ is the function proposed by Businger et al (1971); E is the entrainment (detrainment) as result of mixing layer growth. The concentration is calculated by linear interpolation of pollutant concentration; R stands for material production or loss via chemical reaction. The most widely used chemical scheme for urban photochemestry is the Carbon Bond-IV mechanism (CB-IV). In LOTOS-EUROS, CBM-IV and CB99 by Adelman (1999) are utilized; Q is emission from input emission inventory; D and W are the rest terms are dry and wet deposition. Dry deposition velocity is parameterized by resistance approach,

$$V_d(z) = \frac{1}{R_a(z-d) + R_b + R_c} \tag{1.18}$$

, where R_a, R_b and R_c is aerodynamic resistance, viscous sub-layer resistance and surface resistance. Whereas, the wet deposition is simplified due to limited information of clouds, only cloud scavenging is involved.

The continuity equation is solved by operator splitting method, by calculating concentration changes in first half of each time step, following the sequence of chemistry, diffusion and entrainment, dry deposition, wet deposition, emission and advection; in the second half the order is reversed.

1.3.4 Chemistry

Ozone is one of the most import atmospheric components, involved thousands of chemical reactions. It is impossible to provide a complete description of all these compounds and reactions is impossible. Thus, the solution in LOTOS-EUROS is a lumped structure approach. That is through the lumping of species or reactions utilizing assumptions, e.g. steady state for some radicals [Schaap et al.(2005b)].

The chemical mechanism that is in use for representing urban photochemistry in LOTOS-EUROS is the Carbon Bond-IV (CB-IV). The scheme contains 28 species and 66 reactions, including 12 photochemical reactions. The photolysis reaction consider the solar zenith angle (θ),

$$j = Ae^{\frac{B}{cos(\chi_0)}} \tag{1.19}$$

, where A and B are constant coefficients; the unit is [s^{-1}]. For photo-dissociation of NO_2 (Reaction. 1.5b), the values are 1.45×10^{-2} and -0.4, respectively. For thermal reaction, the temperature correction is applied to reaction rate coefficients,

$$k = Ae^{\frac{-E}{RT}} \tag{1.20}$$

, where A is the pre-exponential factor; E is the activation energy; R is the gas constant; T is the absolute temperature; the unit is [$cm^3 molec^{-1} s^{-1}$]. For Reaction. 1.5a, the A and $-E/R$ are 2.0×10^{-12} and -1400, respectively. Although the reaction rate coefficients is updated regularly, the CB-IV mechanism has been tested against the results of comparisons with other mechanisms and showed good agreement [Schaap et al.(2005b)].

1.4 Research question

Summarily, the core of air pollutant dispersion models is to solve the transport equation, either analytically or numerically, either to solve ODEs or PDEs. The choice of models is a trade-off between accuracy, computational cost, and the ability to prescribe boundary conditions, depends on specific scenarios. For meso-scale to macro-scale, the Lagrangian and Eulerian models are more feasible due to less computation time for the whole domain. If the simulation domain is near source, the Lagrangian models are more efficient. For urban scale cases, LES-based models overwhelm others due to its capability to simulate turbulence over a certain temporal and length scale, instead of using empirical diffusion coefficient for all scales.

Current air quality models that are widely applied to the Netherlands are mainly K-theory based. The representative one is LOTOS-EUROS, a Eulerian chemical transport model. An independent aerodynamically based air quality model for a urban scale is missing from the mainstream. Its development and the potential benefits to improve estimate the vertical profile and surface level concentration of air pollutants, which is a long-term research objective in this field.

This thesis describes the first step to develop a LES-based air pollutants dispersion model by nesting a Large Eddy Simulation model in LOTOS-EUROS domain, to see the influence of turbulent dynamics on concentration fields, to assess the added values of such a model in improving satellite measurement retrievals over urban regions (e.g. by providing realistic profile shapes), and to investigate what relations between ground-based and satellite observations can be expected in a region with scattered sources (e.g. by exploring the representativeness of the slab averaged domain by scattered points.).

Chapter 2

Data processing and preparation for the simulation

This chapter starts with the introduction of Large Eddy Simulation model employed in this thesis, DALES, including the dynamics, the chemical scheme and the emission sources. As a nesting framework, the boundary conditions that os determined by LOTOS-EUROS will be explicitly explained. The meteorological inputs for DALES is so complex that is introduced separately. An additional interface model CLASS, which solves the same governing equation and provides similar results as DALES, is used to assist parts of academic experiments in the following chapters. The final part will describe how the meteorological cases are chosen for DALES simulation.

2.1 Region and cases of interest

The region of interest (ROI) in DALES for simulation over Rotterdam is the area between 51.85° N and 51.96 ° N, 4.35° E and 4.6° E. The ROI covers the whole city center of Rotterdam.

The simulation of DALES will be evaluated by both LOTOS-EUROS and observations. The main criteria to pick out date of interest is the availability of observational data. This thesis employs Ozone Monitoring Instrument (OMI) satellite. The OMI uses hyper-spectral imaging to observe solar backscattered radiation by the atmosphere and surface. It covers band from the visible to ultraviolet band (270 to 500 nm, spectral resolution of 0.5 nm). The nadir push-broom mode ensures large swath of the OMI that can cover the entire earth daily with a viewing angle of 114°, equaling to 2600 km swath at surface. The ground pixel size for urban-scale is around 13 $km\times$ 24 km in the normal global operation mode. In the zoom mode the resolution reaches 13 $km\times$ 12 km. As the successor of TOMS, SBUV, GOME and SCIAMACHY, the OMI records for total ozone and other atmospheric parameters related to ozone chemistry and climate, including nitrogen dioxide (NO_2), sulfur dioxide (SO_2), hypobromite (BrO), chlorine dioxide ($OClO$) and aerosol characteristics. The data product in this thesis is DOMINO (Dutch OMI NO_2 data), which is post-processed based on OMI level 2 orbital swaths data [Boersma et al.(2011)]. In the OMI data products, the tropospheric NO_2 slant column density (N^S) is measured once a day, at local equator crossing time between 13 p.m. and 14 p.m.. The measured tropospheric N^S is further converted into tropospheric vertical column density (N^V) by considering the simulated tropospheric air mass factor (AMF) from TM4 (Equation. C.19).

The chosen cases of interest should be having available data on the one hand, and less cloudy within the ROI. Based on these requirements, totally four days are chosen, including two winter days 12th (Saturday) and 16th (Wednesday) of November in year 2011 and 2nd (Saturday) and 26th (Tuesday) of June in year 2012. Concisely, the four cases refer to W1, W2, S1 and S2. Figure. 2.1 present the DOMINO data product of these four cases. The whitish pixel indicates the amount of clouds. The more white the pixel, more cloudy over this area. Among all the cases, the data quality of case S2 is the best, with the highest resolution and less clouds at measuring time.

But the OMI observations only provides the information when the satellite flies over ROI, which is at around 14:00 p.m. of local time. Therefore, in-situ measurement is necessary to study the time temporal variation of cloud fraction. The local observation data is from KNMI weather station at Rotterdam (station number 344) . According to Figure. 2.2, the local measurements at 14:00 show good agreement with satellite data. The cloud cover during the majority of daytime is lower than 4 (sky half cloudy) in most of the cases, especially the two winter days where the sky is almost clear. The data from case S1 is more cloudy compared with other selections. The local observation proves the selected dates based on OMI data availability are suitable for the following research.

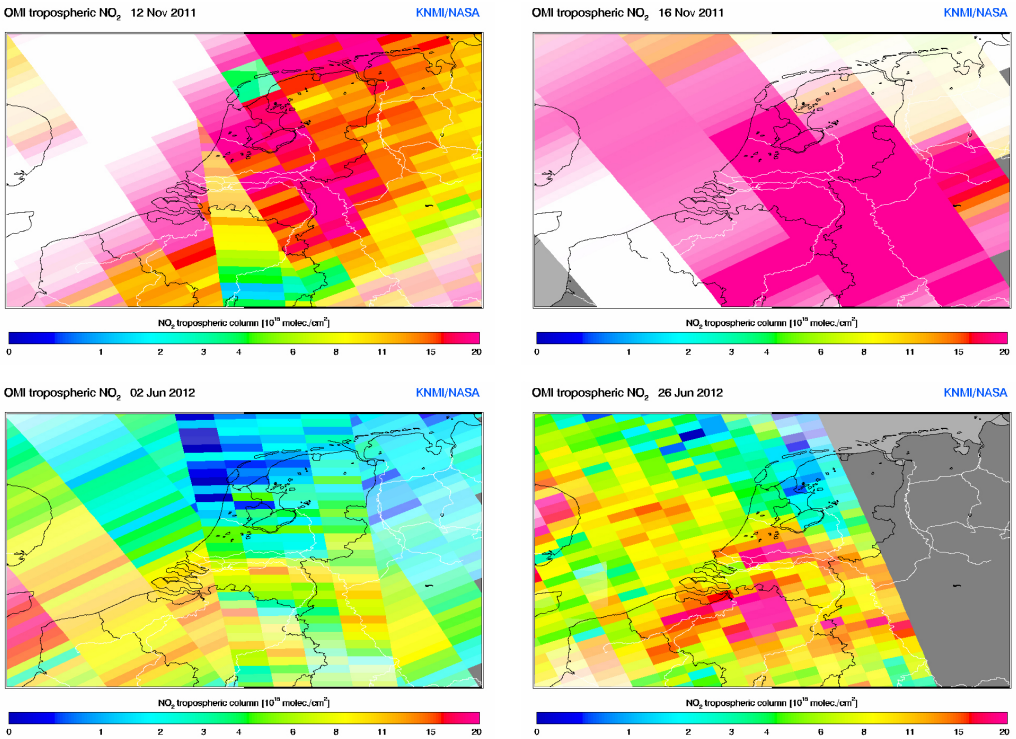

Figure 2.1: DOMINO data of cases of interest. From top to bottom, left to right is the case W1 (12th-November-2011), W2 (16th-November-2011), S1 (02nd-June-2012) and S2 (26th-June-2012). The different swath directions in case W1 and S1 are because the data is combined of different orbits.

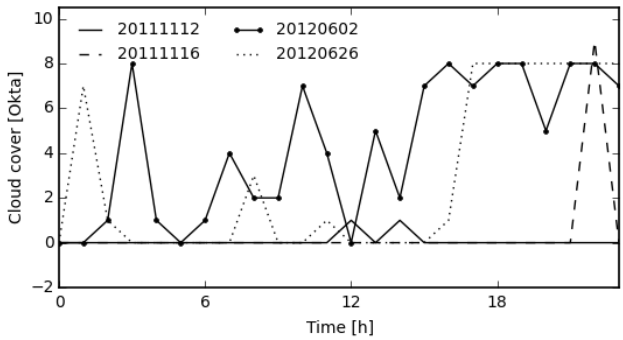

Figure 2.2: KNMI weather station cloud cover in [Okta] over Rotterdam region.

2.2 Dutch atmospheric large eddy simulation (DALES)

The high resolution model employed in the nesting framework is the Dutch Atmospheric Large Eddy Simulation (DALES), version 4.1, which is currently maintained by researchers from Delft University of Technology, the Royal Netherlands Meteorological Institute (KNMI), Wageningen University and the Max Planck Institute for Meteorology [Heus et al.(2010)]. As a large eddy simulation, DALES resolves the filtered Navier-Stokes equation under Boussinesq approximation. In practice, the filter width is set to be the grid size of the LES. The filtered

governing equations are,

$$\frac{\partial \widetilde{u}_i}{\partial x_i} = 0 \tag{2.1a}$$

$$\frac{\partial \widetilde{u}_i}{\partial t} = -\frac{\partial \widetilde{u}_i \widetilde{u}_j}{\partial x_j} - \frac{\partial \pi}{\partial x_j} + \frac{g}{\theta_0}\widetilde{\theta}_v \delta_{i3} + F_i - \frac{\partial \tau_{ij}}{\partial x_j} \tag{2.1b}$$

$$\frac{\partial \widetilde{\phi}}{\partial t} = -\frac{\partial \widetilde{u}_j \widetilde{\phi}}{\partial x_j} - \frac{\partial R_{uj,\phi}}{\partial x_j} + S_\varphi \tag{2.1c}$$

, where the tilde $\widetilde{(\cdot)}$ indicates averaged within filter width; π is the modified pressure; δ_{ij} is the Kronecker delta; e is the sub-filter scale turbulence kinetic energy (SFS-TKE); F_i is other forcings, including large scale forcings and Coriolis acceleration (Equation.2.3); τ_{ij} is the deviatoric part of the sub-grid momentum flux (Equation.2.4); Ω is the Earth angular velocity; S_φ is the source term for scalars, including micro-physics, radiative, chemical, large-scale forcing and relaxation terms; the molecular diffusion term is neglected in DALES [Heus et al.(2009)].

$$\pi = \frac{\widetilde{p}}{\rho} + \frac{2}{3}e \tag{2.2}$$

$$F_i^{cor} = -2\epsilon_{ijk}\Omega_j \widetilde{u_k} \tag{2.3}$$

$$\tau_{ij} \equiv \widetilde{u_i u_j} - \widetilde{u}_i \widetilde{u}_j - \frac{2}{3}e \tag{2.4}$$

$$e = \frac{1}{2}(\widetilde{u_i u_i} - \widetilde{u}_i \widetilde{u}_i) \tag{2.5}$$

The sub-filter scale turbulence is parameterized on basis of K-theory, namely diffusion coefficients K_h and K_m (Equation.2.6 2.7). Two methods are employed to estimate diffusivity coefficients, either applying SFS-TKE moddel, which is default in DALES, or Smagorinsky closure [Heus et al.(2010)].

$$R_{u_j,\phi} = -K_h \frac{\partial \widetilde{\phi}}{\partial x_j} \tag{2.6}$$

$$\tau_{ij} = -K_m\left(\frac{\partial \widetilde{u}_i}{\partial x_j} + \frac{\partial \widetilde{u}_j}{\partial x_i}\right) \tag{2.7}$$

2.2.1 General setting and input

The compulsory inputs of DALES include general model setting (namoptions), initial profiles (prof.inp) and large scale forcing (lscale.inp). Others are optional, such as scalars (scalar.inp), time-dependent large scalar flux (ls_flux.inp), scalar flux (sv_flux.inp) and chemical system (chem.inp). Since DALES itself is not exclusively designed for air pollution dispersion modeling. Consequently, this thesis is aim to develop an air pollution dispersion module for

DALES. The new developed module requires boundary condition constrained by LOTOS-EUROS for passive scalars (svb.inp) and heterogeneous surface emission sources (src.inp). These inputs are either derived from meteorological datasets or concentration fields of LOTOS-EUROS, which will be introduced in the following sections.

2.2.2 Boundary conditions for passive scalars

Embedded in the DALES, the periodic boundary condition (PBC) is applied to horizontal boundaries. That is, the outflow of quantities from one side will become the inflow at opposite, as shown in Figure.2.3. The PBC is useful foe academic studies, because it This default boundary scheme should be avoided by passive scalars. Otherwise, the full domain would be polluted without outlet for pollution, which is unrealistic and mislead the following analysis. Instead, a boundary constrained by the LOTOS-EUROS via nesting model approach (Figure. 2.4) is used as the boundary condition for passive scalars. Nesting model is a framework consisting of a large scale model with coarse resolution and a model for local scale with high resolution. The regional model carries out simulations on large scale, then the output is used to drive the high resolution model over region of interest (ROI).

In this thesis, the regional and local model of nesting framework are LOTOS-EUROS and DALES, respectively. The horizontal boundary conditions of DALES are set to be stagnation point for passive scalars outflow, which is zero. The inflow at boundary is derived from the concentration fields of LOTOS-EUROS. As a result, the outflow of DALES would not enter the DALES domain again, meanwhile the surrounding large scale impacts are taken into consideration. In operation, firstly a ROI is selected from LOTOS-EUROS data according to DALES setting, in this thesis is the central Rotterdam region, which will be explained in Section 2.4. The boundary values are chosen from the pixels of LOTOS-EUROS at the outside boundary of the ROI. The boundary conditions are further interpolated to be consist with DALES domain size. Then the grid cells at outermost ih/jh columns/lines (ih and jh are the number of x-directional and y-directional ghost points, respectively) in DALES computation domain are set with values of the 4 boundaries of processed ROI concentration fields. This boundary condition is updated hourly, consequently, a time dependent passive scalar boundary condition controlled by LOTOS-EUROS concentration fields is setup.

2.2.3 Heterogeneous air pollutants emission

The surface emission of air pollutants is strongly spatial and temporal dependent. Instead of a uniform surface emission for the whole domain, which is applied to DALES, the heterogeneous surface emission data comes from URBIS traffic emission inventory. The LOTOS-EUROS emission inventory MACC(III) is not available, so the URBIS is in use. URBIS is developed by TNO that calculates the annual average concentration of various air pollutants in real-time. It simulated the concentration via Gaussian plume dispersion model on a typical resolution of 100 $m\times$ 100 m for real-time analysis. The inventory of URBIS includes annual average emissions from inhabitants, industry and local sources and emissions from shipping and land transport.

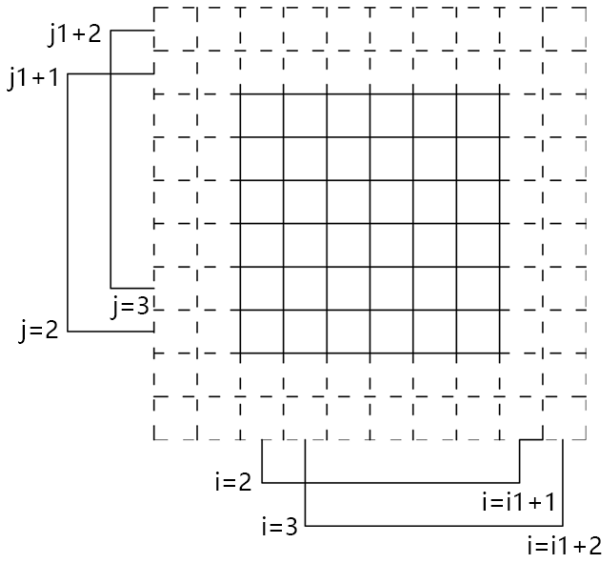

Figure 2.3: Periodic boundary scheme for DALES horizontal boundary conditions. The dashed area is the ghost domain in DALES. Here shows one processors as an example. Assume the number of ghost grid is 2, the value of the first column (column 2) of the real domain is passed to the column $i1 + 1$, the first column of the ghost domain at the right boundary. Similarly, the line 2 of the real domain is passed to the line $j1 + 1$ that is located at the ghost domain. For multiple processors, this boundary condition is operationally realized by Message Passing Interface (MPI).

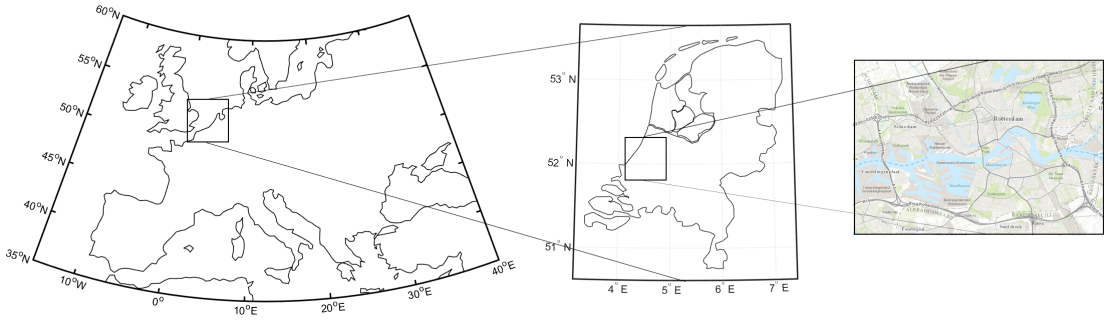

Figure 2.4: Concept of nesting model approach. Use a coarse resolution model to carry out simulations of large region, then employ the output to drive a high resolution over an area of interest.

In this thesis, only the land traffic emission of URBIS emission inventory is available and therefore is the only sources applied. The given air pollutants are nitrogen oxides (NO_2 and NO_x), particulates matter (PM10 and PM2.5), ammonia (NH_3) and element carbon. According to the chemistry scheme, only information about NO_x is necessary. Since NO is directly emitted from vehicles, only the NO emission at the surface is applied, which is calculated by subtracting NO_2 emission from total NO_x emission.

In this emission inventory, each emission source (I, [$\mu g m^{-1} s^{-1}$]) represents for a specific section of a road (Figure.2.5). The emission is normalized by the corresponding length of

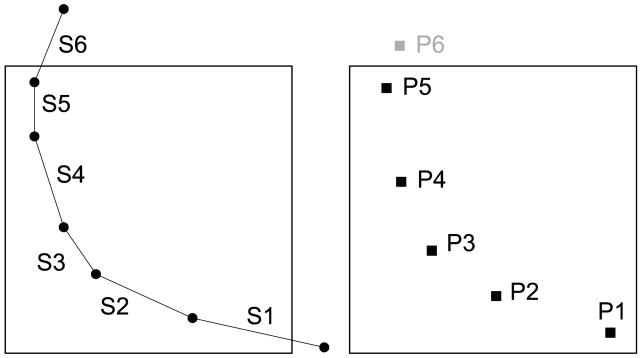

Figure 2.5: Deployment of emission sources. • is the node for each road section. As shown in the figure, For a road with five sections distributed in DALES domain, the middle point is then calculated to represent the road section. The emission would be removed if the computed middle point is out of DALES domain, e.g $P6$.

road section length. When applying to the DALES domain, a emission source need to be converted into form with unit of [$\mu gm^{-1}s^{-1}$] into [$ppbs^{-1}$] (Equation.2.8),

$$E = I \times L \times \frac{V_m}{M_{NO}} \times \frac{1}{V_{DALES}} \tag{2.8}$$

, where L means the length of road section; V_m is the standard molar volume of ideal gas (22.71108 [$Lmol^{-1}$]); M_{NO} is the molar mass of NO (30.01 [$gmol^{-1}$]); V_{DALES} is the volume of each DALES grid cell. So far, the heterogeneous emission inventory for DALES is completed. But the traffic emission is not supposed to be constant with time, and could be varies in seasons. In URBIS, the emission of a particular hour is calculated by applying the scaling factor that associates emission at that hour with current meteorology. Later taking actual traffic counts into consideration makes the model a more real-time application. In this thesis, however, to be consist with LOTOS-EUROS as much as possible, the factor applied to MACC(III) traffic emission inventory is in use. According to Figure. 2.6, the factor in summer time is generally higher than winter time, with two peaks at June and September. Within a week, the scaling factor increases from Monday to Friday, followed by a sudden drop during weekend. The diurnal cycle of factors shows a more clear pattern with two strong peak at morning and afternoon rush hours (8-9 a.m. and 17-18 p.m., respectively).

Not only the emission sources themselves, locations of sources are also need to calculate when they are deployed to DALES. According to Figure. 2.5, firstly, calculating the geometric middle point of each road section (Equation.2.9a and 2.9b),

$$x_m = \frac{x_1 + x_2}{2} \tag{2.9a}$$

$$y_m = \frac{y_1 + y_2}{2} \tag{2.9b}$$

, where x and y are horizontal coordinates; subscript 1, 2 and m means the first node, the second node and the middle point of a road section. Then updated coordinates will be deployed into the DALES domain.

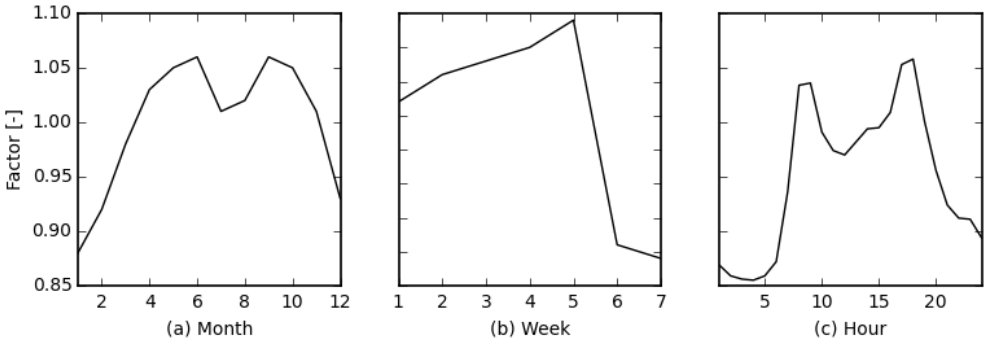

Figure 2.6: Time dependent emission factors. (a) monthly factors. The maximum value is at summer period; (b) weekly factors. The low values are at weekend; (c) hourly factors. Two peaks show up at morning and afternoon rush hours. (Factor source: [Schaap et al.(2005a)]).

2.2.4 Chemistry module

The chemistry module in DALES, the atmospheric compounds disperse as passive scalars, with involvement of chemical reactions (Equation.2.10).

$$S_{\varphi_1} = P(t, \varphi_m) - L(t, \varphi_m)\varphi_1 \qquad m = 1, ..., n. \tag{2.10}$$

, where $P(t, \varphi_m)$ and $L(t, \varphi_m)$ are the production and loss for component φ_1; n represents the number of species. The chemical scheme in DALES is numerically solved by TWOSTEP solver, which uses an implicit second-order accurate method based on the two-step backward differentiation formula [Heus et al.(2010)].

The reaction rate coefficients (k) depends on temperature or radiation, therefore, called k_T and k_R, correspondingly. According to the chemical module in DALES [de Arellano et al.(2011)], the temperature effect is including by correction of absolute temperature. Similarly, by including the solar zenith angle (SZA, χ_0), which is derived from local latitude, date and time (Equation. C.12), the radiation dependency is considered. In the nighttime, there is no photolysis, the k_R is zero.

Besides, the presence of clouds also affect the actinic flux and therefore indirectly affects k_R. If there is liquid water in the domain, namely clouds exist, then the maximum χ_0 is cutoff to 60°. Clouds in chemical module fall into two categories. If the optically depth of clouds (τ_c, Equation.C.13) is less than 5 (τ_{c0}), then clouds are optically thin and its influence is negligible. Otherwise, the cloud is considered to be optically dense and additional correction factors are applied to the temperature or radiation dependent (k_T or k_R) [Chang et al.(1987)] [de Arellano et al.(2011)]. Here they are collectively referred to as k_{clear},

$$k_{cloud} = k_{clear}[1 + a(F - 1)] \tag{2.11}$$

, where k_{cloud} and k_{clear} are the reaction rate coefficients under cloudy and clear sky , respectively; a is the cloud coverage fraction; F is the ratio of the cloudy sky to clear sky photolysis rate coefficient, depends on the depends on the relative location between the

height where the reaction happens and the clouds [Chang et al.(1987)]. For each grid point, if the reaction happens below the cloud layer,

$$F_b = 1.6 \cdot tr \cdot \cos\chi_0 \tag{2.12}$$

, where tr is the transmission coefficient (Equation. C.14); When the reaction occurs above the cloud layer, the F depends on chemical species,

$$F_a = 1 + \alpha \cdot (1 - tr) \cdot \cos\chi_0 \tag{2.13}$$

, where α is a reaction dependent coefficient; inside of the clouds, the factor is calculated iteratively by two neighboring layers from top of the cloud to the bottom, with a weight function described by the fraction of liquid water content,

$$F_{n-1} = F_n - \frac{q_{l0,n}}{q_{sum}}(F_a - F_b) \qquad n = z_{top}, ..., z_{base} \tag{2.14}$$

, where z_{top} and z_{base} mean the top height and base height of cloud, respectively; q_{l0} is the liquid water content of layer n for a certain grid point; q_{sum} is the total liquid water content within cloud layer at the same horizontal location; f_a and f_b are factors under cases when reactions happens above and below cloud respectively. The factor is then applied to k_{eff} directly to add clouds influences.

As mentioned in Section 1.1, the absence of VOCs is the simplest case and employed in this thesis. Here, only two reactions for $NO_x - O_3$ system are simulated in the numerical experiments (Reaction.1.5a and 1.5b). In operation, the non-reactant terms are in parentheses, meaning only O_3 and NO_x are the input passive scalars. The chemical system and reaction rate coefficients are listed in Table. 2.1. The photolysis reaction (R1) is radiation dependent and thermal reaction (R2) is temperature corrected. Both reactions are perturbed by the clouds.

Table 2.1: $NO_x - O_3$ equilibrium chemical scheme. The reaction rate coefficients refer to the default value in DALES [de Arellano et al.(2011)] [Schofield(1967)]. T is the absolute temperature ([K]); χ_0 is the solar zenith angle ([$\circ$]).

Reaction name	Reaction rate coefficient	Radiation dependent	Chemical reaction
R1	$3.00 \times 10^{-12} \cdot e^{\frac{-1500}{T}}$	No	$NO + O_3 \rightarrow NO_2 + (O_2)$
R2	$1.67 \times 10^{-2} \cdot e^{\frac{-0.575}{\cos(\chi_0)}}$	Yes	$NO_2 + hv \rightarrow O_3 + NO$

2.3 CLASS

Chemistry Land-Surface Atmospheric Soil Slab (CLASS) is a model associated with the book Atmospheric Boundary Layer [de Arellano et al.(2015)]. In short, the CLASS covers the main contents covering atmospheric physics and dynamics, atmospheric chemistry, physics of land surface and bio-chemistry system. The CLASS gives a quantitative description of the behavior of different meteorological parameters by solving budget equations. The budget equation describes the temporal evolution of variables, considering influences of surface, processes within boundary layer, interactions between boundary layer and upper layers, and effects of horizontal advections.

Compared with DALES, CLASS solves the same governing equation and provides similar averaged results. For simple academic experiments, CLASS is is easier to use and more efficient. This model is employed to simulate the sensitivity of NO_2 concentration to background ozone level in Section 3.1.3.

2.4 Meteorological data

There are two meteorology data sets available to run the DALES simulation. The one that also employed by LOTOS-EUROS is European Center for Medium-Range Weather Forecasts (ECMWF) ERA-Interim. It is a global atmospheric reanalysis covering from 1979 onwards, and continuously updated in real time. The ERA-Interim applies data assimilation system based on a 2006 release of the Integrated Forecast System (IFS) (Cy31r2), which contains a 4-dimensional analysis with 12-hour analysis window. The model grid is at T255 spectral resolution (around 0.75°, 80 km) and 60 vertical levels from surface up to 0.1 hPa. This thesis uses hourly atmospheric fields on pressure levels, with analysis and forecast surface fields at step 0 and 6 respectively [Berrisford et al.(2011)] [Dee et al.(2011)]. The parameters chosen are presented in the Table.2.3.

In ECMWF, for pressure levels model, the pressure coordinate needs to convert into height profile with Equation.2.15,

$$\widetilde{z} = -Hln(\frac{P}{P^*}) \tag{2.15}$$

, where $\widetilde{z}$ is the adapted height coordinate; H is the typical height of region of interest; P^* is the reference pressure. In this thesis, the H and P_0 are 7 km and 1013 hPa respectively. The temperature from ECMWF should be also converted into potential temperature and further into liquid water potential temperature by Equation.2.16 and 2.17,

$$\theta = T(\frac{P_0}{P})^{R_d/C_p} \tag{2.16}$$

$$\theta_l \approx \theta - \frac{L_v}{C_p(\frac{P}{P_0})^{R_d/C_p}} q_c \tag{2.17}$$

, where θ is the potential temperature; T and P are the absolute temperature and pressure; P_0 is the reference pressure; R_d is the gas constant for dry air; C_p is the heat capacity for dry air; L is the latent heat from vaporization; q_c is the cloud liquid water content specific humidity. The vertical wind velocity should be further converted into unit of [m/s] (Equation.2.18),

$$w_s = \frac{w}{-\rho g} \tag{2.18a}$$

$$w = \frac{dP}{dt} \tag{2.18b}$$

$$w_s = \frac{dz}{dt} \tag{2.18c}$$

, where the P and z are pressure and height profile; t is the time; ρ is air density; g is the acceleration due to gravity; w_s is the transfered vertical velocity and treated as large scale subsidence. The surface heat flux and moisture flux are converted from sensible heat flux and latent heat flux, respectively (Equation.2.19 and 2.20).

Table 2.2: Table of constants.

Parameter	Symbol	Value	Unit	Description
Reference pressure	P^*	1013	$[hPa]$	Reference pressure to convert pressure coordinate to height cordinate
Typical height of region of interest	H	7	$[km]$	
Reference pressure	P_0	1000	$[hPa]$	Reference pressure to calculate the potential temperature
Gas constant for dry air	R_d	287.0	$[Jkg^{-1}K^{-1}]$	
Heat capacity for dry air	C_p	1004	$[Jkg^{-1}K^{-1}]$	
Latent heat from vaporization	L_v	2.5×10^6	$[Jkg^{-1}]$	
Gravity acceleration	g	9.8	$[ms^{-2}]$	
Air density	ρ	1.225	$[kgm^{-3}]$	

$$\widetilde{w'\theta'_s} = \frac{sshf}{\rho C_p dt} \tag{2.19}$$

$$\widetilde{w'q'_s} = \frac{slhf}{\rho L_v dt} \tag{2.20}$$

, where the $\widetilde{w'\theta'_s}$ and $\widetilde{w'q'_s}$ are surface heat flux and moisture flux; $sshf$ and $slhf$ represent the surface sensible and latent heat flux, correspondingly; ρ is the density; C_p is the heat capacity for dry air; dt is the period during which the surface sensible or latent heat flux is integrated; L_v is the latent heat from vaporization. All these constant parameters are presented in Table.2.2.

Although ECMWF can prescribe most of the initial parameters in DALES, the temporal and spatial resolution is rather coarse. Besides, some of the large scale forcing terms are missing from this dataset, such as geostrophic wind (ug and vg). Despite usually these parameters can be set to zero. An alternative meteorological condition is the Regional Atmospheric Climate Model (RACMO). This model was developed by Royal Netherlands Meteorological Institute (KNMI) in cooperation with Danish Meteorological Institute, based on High Resolution Limited Area Model (HIRLAM) numerical weather prediction model. In the latter versions of RACMO, the HIRLAM dynamical core and ECMWF IFS physics are combined. The RACMO data used applies IFS CY31r1 cycle at KNMI-mast Cabauw, the Netherlands [Meijgaard et al.(2008)]. Compared with ECMWF, the RACMO is more compatible with DALES. The parameters of RACMO used as inputs of DALES are listed in Table. 2.4.

The two meteorological inputs are serves different purposes. The ECMWF, which is also the meteorological driver in LOTOS-EUROS, is applied to simulation over Rotterdam

Table 2.3: Meteorological parameters from ECMWF. The pressure levels provides the profile information at every 6 hours; surface model consists of analysis data at every 12 hours (step 0) and forecast data at every 6 hours (step 0).

Model type	Parameter	Symbol	Unit	Description
Pressure levels	Pressure	p	$[mbar]$	Pressure profile, used to calculate the height profile
	Temperature	t	$[K]$	Temperature profile, need to be converted into liquid water potential temperature
	Specific cloud liquid water content	clwc	$[kgkg^{-1}]$	Part of the total humidity
	Specific humidity	q	$[kgkg^{-1}]$	Part of the total humidity
	U component of wind	u	$[ms^{-1}]$	Wind velocity in x-direction
	V component of wind	v	$[ms^{-1}]$	Wind velocity in y-direction
	W component of wind	w	$[Pas^{-1}]$	Used to calculate the vertical wind velocity in unit of $[ms^{-1}]$
Surface	Surface pressure	sp	$[Pa]$	
	Surface temperature	st	$[K]$	
	Surface sensible heat flux	sshf	$[Jm^{-2}]$	Used to calculate the surface heat flux in unit of $[Kms^{-1}]$
	Surface latent heat flux	slhf	$[Jm^{-2}]$	Used to calculate the surface moisture flux in unit of $[kgkg^{-1}ms^{-1}]$
	Boundary layer height	blh	$[m]$	Time dependent boundary layer height

region in Section 3.2. The missing large scale forcing parameters are derived from RACMO. While the RACMO is only used for academic sensitivity study in Section 3.1. In operation, either from ECMWF or RACMO, the slab averaged initial profiles of the ROI are linearly interpolated into prescribed height profile in DALES.

Table 2.4: Meteorological parameters from RACMO.

Parameter	Symbol	Unit	Description
Pressure	pressure_f	$[Pa]$	Pressure at full level height
Temperature	t	$[K]$	Temperature profile, need to covert into liquid water potential temperature
Water vapor mixing ratio	q	$[kgkg{-}1]$	Parts of the total water specific humidity
Liquid water mixing ratio	ql	$[kgkg^{-1}]$	Parts of the total water specific humidity
U component of wind	u	$[ms^{-1}]$	
V component of wind	v	$[ms^{-1}]$	
U component of geostrophic wind	ug	$[ms^{-1}]$	Pressure profile, used to calculate the height profile
V component of geostrophic wind	vg	$[ms^{-1}]$	Wind velocity in y-direction
Vertical pressure velocity	omega	$[Pas^{-1}]$	Need to covert into unit of $[ms^{-1}]$
Surface pressure	ps	$[Pa]$	Derived from the pressure profile
Surface temperature	ts	$[K]$	Derived from the temperature profile
Surface sensible heat flux	wtsurf	$[Wm^{-2}]$	Need to convert into unit of $[Kms^{-1}]$
Surface latent heat flux	wqsurf	$[Wm^{-2}]$	Need to convert into unit of $[kgkg^{-1}ms^{-1}]$

Chapter 3

Results and discussion

As a new developed air quality model based on large eddy simulation, a basic acknowledge of the properties of DALES atmospheric dynamics and chemistry scheme is necessary. Hereto in this chapter, several academic experiments are performed to explore the sensitivity of nitrogen dioxide (NO_2) concentration. Based on this general idea how the concentration field evolves in DALES, the simulation over Rotterdam region is then carried out under four typical cases selected based on Section 2.1. These results would be further evaluated by observational data and compared with corresponding LOTOS-EUROS simulation in spatial and temporal pattern.

3.1 Sensitivity study to meteorology and chemistry of nitrogen dioxide concentration field

As a Large Eddy Simulation model, DALES is powerful enough to carry out sensitivity study in both dynamics and chemistry. There are many parameters in DALES that perturb the NO_2 concentration. Meteorological processes such as clouds and turbulent mixing would have direct influence either on NO_2 concentration field, or indirect impact on reaction rate coefficients. From the chemistry itself, the NO_2 concentration is directly related to the background ozone level and reaction rate coefficients, which will be explained in detail. Conclusively, in this part, several representative parameters featuring DALES would be selected to study the NO_2 concentration field sensitivity.

The initial condition chosen as the control case C0 is the summer case S2 (26th June of year 2012 (Tuesday)). The reason for choosing this day is that the convection is stronger due to more radiation in summer days meanwhile the clouds is much less compared with case S1 (Figure. 2.2). The initial profiles of meteorological parameters and reactants are from RACMO and LOTOS-EUROS concentration, respectively. The whole parameter initial settings for DALES are presented in Table. 3.1 and Figure. 3.1. The surface heat flux $\overline{w'\theta'}$ used here is the mean value from 6.a.m. to 18 p.m., to drive the boundary layer development. Note for NO, a homogeneous surface emission is applied to see the temporal evolution of concentration. Unless specified, all the values of parameters in DALES that should be referred to control case C0 in this section.

The dynamics evolution of control case C0 is illustrated in Figure. 3.2. It is clear to see the growth of boundary layer. The cloud layer locates at around 1500 m high at 12 p.m., and the liquid water content decreases gradually afterwards.

The chemical mechanism used is the equilibrium scheme (Table. 2.1) as mentioned in Table. 2.1, the reaction rate coefficients are either radiation or temperature dependent. To concisely describe the concentration variation of NO_2, a concept of NO_2 fraction in total

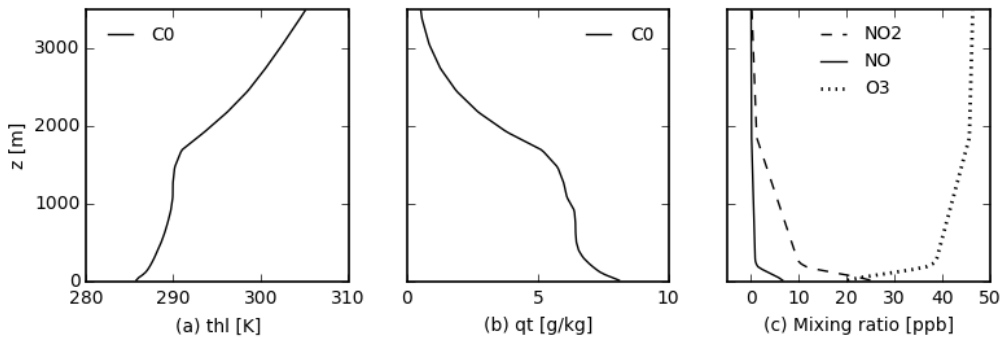

Figure 3.1: Initial profiles of control case C0. (a) liquid water potential temperature (θ_l); (b) total water specific humidity (q_t); (c) chemical reactants concentration of NO_x and O_3.

Table 3.1: Parameters in DALES for control case C0. The reaction rate coefficients are referred to [1] [de Arellano et al.(2011)]; [2] [Schofield(1967)].

Parameter	Value	Unit	Description
runtime	43200	$[s]$	Simulation time (12 hours)
itot	64	-	Total grid points in x-direction
jtot	64	-	Total grid points in y-direction
xsize	3200	$[m]$	Dimension of domain in x-direction
ysize	3200	$[m]$	Dimension of domain in y-direction
kmax	100	-	Number of layers in vertical direction; the vertical layer ranges from 17.5 m to 3500 m, with spacing of 35 m
xlat	51.91	$[\circ]$	Latitude of center of Rotterdam center
xlon	4.48	$[\circ]$	Longitude of center of Rotterdam center
xday	178	-	Day of the year
xtime	4	$[h]$	Start time (UTC, the local time is 6 a.m. due to daylight saving time)
thls	285.764	$[K]$	Surface liquid water potential temperature
ps	102118.0	$[Pa]$	Surface pressure
$\overline{w'\theta'}$	0.0629	$[Kms^{-1}]$	Surface heat flux
$\overline{w'q'}$	0.0121	$[gkg^{-1}ms^{-1}]$	Surface moisture flux
$\overline{w'c'_{NO}}$	0.1	$[ppbms^{-1}]$	Surface flux of NO
j	$1.67 \times 10^{-2} \times e^{\frac{-0.575}{\cos(\chi_0)}}$ [1]	$[s^{-1}]$	Photolysis rate coefficient (first order reaction rate coefficient), corrected for radiation
k	$3.00 \times 10^{-12} \times e^{\frac{-1500}{T}}$ [2]	$[cm^3 molec^{-1} s^{-1}]$	Thermal reaction rate coefficient (second order reaction rate coefficient), corrected for temperature
lcloudKconst	false	-	Clouds perturbed reaction rate coefficients

amount of NO_x is introduced based on Leighton ratio relationship (Equation. 3.1a),

$$L = \frac{[NO]}{[NO_2]} = \frac{j}{k[O_3]} \tag{3.1a}$$

$$F_{NO_2} = \frac{[NO_2]}{[NO_x]} = \frac{1}{1+L} = \frac{1}{1+\frac{j}{k[O_3]}} \tag{3.1b}$$

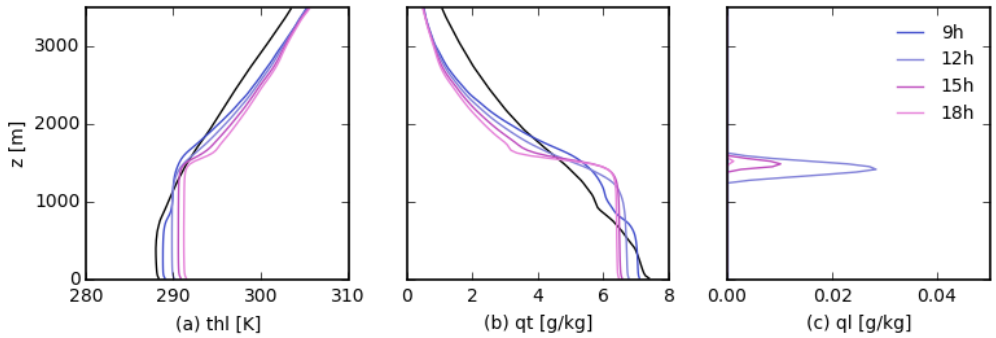

Figure 3.2: Evolution of 10-minute slab averaged dynamics of control case C0. (a) liquid water potential temperature (θ_l); (b) total water specific humidity (q_t); (c) liquid water specific humidity (q_l). The black line indicates the initial profile.

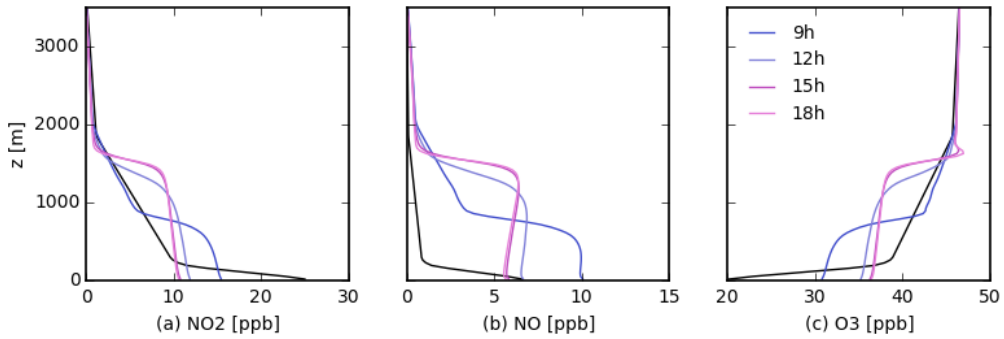

Figure 3.3: Evolution of 10-minute slab averaged concentration field profile of control case C0. (a) NO_2 concentration; (b) NO concentration; (c) O_3 concentration. The black line indicates the initial profile.

It is clear that the NO_2 fraction (F_{NO_2}) in total NO_x directly depends on the background ozone level ([O_3]), the photolysis rate (j) and the thermal reaction rate (k).

The time evolution of concentration fields of control case C0 is presented in Figure. 3.3. The concentration fields growth is highly consistent with boundary layer evolution. The reactants are well-mixed vertically within the boundary layer. At the height where clouds form, the concentration vertical transport is enhanced by release of latent heat in the clouds, which is also reflected by the NO_2 shape function evolution (Figure. 3.4 (b)). This property will be discussed further in Section. 3.1.1.

Revealed by Figure. 3.4 (a), near the surface, the NO_2 fraction s slightly increases with height due to the NO emission at ground level. Initially, the NO_2 fraction is relatively small within the sub-cloud layer. With the reaction continuing, the NO is consumed quickly by the background ozone. The ground level NO_2 fraction falls in range between 70% and 75%, agreeing with the most cases that NO_2 fraction is around 70% [Beirle(2004)]. Both in the boundary layer and the upper free atmosphere, the NO_x slight shifts to NO with increasing height because the temperature dependency of the second order reaction and higher NO_2 photolysis rate. There is a positive jump of NO_2 fraction at the transition layer, where both

the NO_2 and NO concentration decline strongly. The shape function, on the other hand, presenting a considerable vertical transport by the clouds when comparing to the shape profile at the 9 a.m.

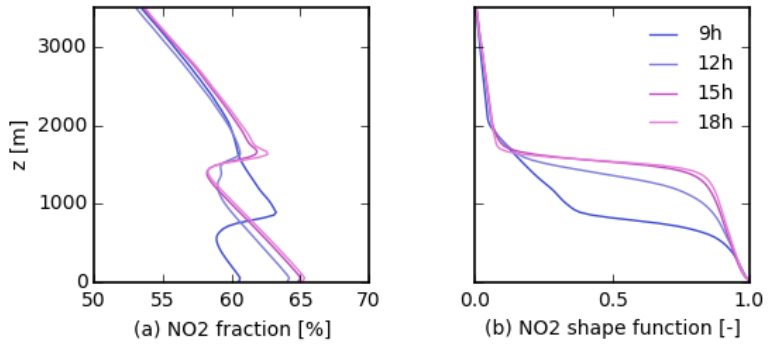

Figure 3.4: Evolution of 10-minute slab averaged Leighton ratio and NO_2 fraction of control case C0. (a) NO_2 fraction. The NO_x is mainly in form of NO_2 in control case C0 due to no correction for reaction rate coefficients; (b) NO_2 shape function.

For a second order reaction (Reaction. 1.5a), the covariance is to study the interaction between two reacting compounds, namely NO and O_3. The concept of segregation intensity of second order reaction is introduced [Ouwersloot et al.(2011)]. The reacting compounds must be mixed before reaction, which is the process controlled by the turbulence. Quantitatively, this segregation is defined as the ratio between the covariance of reactant NO and O_3 and their mean concentration,

$$I_s = \frac{[c'_{NO}c'_{O_3}]}{[\overline{c_{NO}}] \cdot [\overline{c_{O_3}}]} \tag{3.2}$$

There are two distinct turbulent layers under presence of the clouds. In the mixed layer, the I_s is negligible, meaning the compounds are well-mixed by turbulence. On the other hand, in the cloud layer, the segregation is strong because the horizontal gradient between clouds and the environment is significant, that leading to large (absolute) I_s (up to 3%). Despite at 9 a.m. when there is no cloud forming, the large (absolute) I_s shows up at the transition layer due to large gradients at this height.

The sign of I_s depends on the covariance of the reactants, which is the comprehensive result of chemistry and dynamics. If only considering chemistry, for two reacting compounds, the I_s should be smaller than zero because they are negatively correlated, as shown in Figure. 3.5. In control case C0, the positive values correspond to the downward NO flux and upward O_3 flux (Figure. 3.6 (b) and (c)) that reactants are segregated by the clouds.

Based on the analysis of the control case C0, one can conclude that the concentration fields are not only determined by the chemistry, but also influenced by the atmospheric dynamics. Hereto, the sensitivity to these factors is studied, including background ozone concentration in Section 3.1.1, reaction rate coefficient in Section 3.1.2, clouds in Section 3.1.3 and turbulent control in Section 3.1.4.

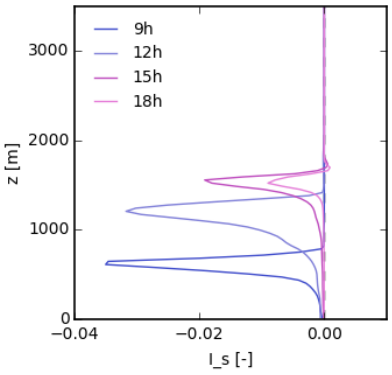

Figure 3.5: Evolution of 10-minute slab averaged resolved segregation of second order reaction of control case C0.

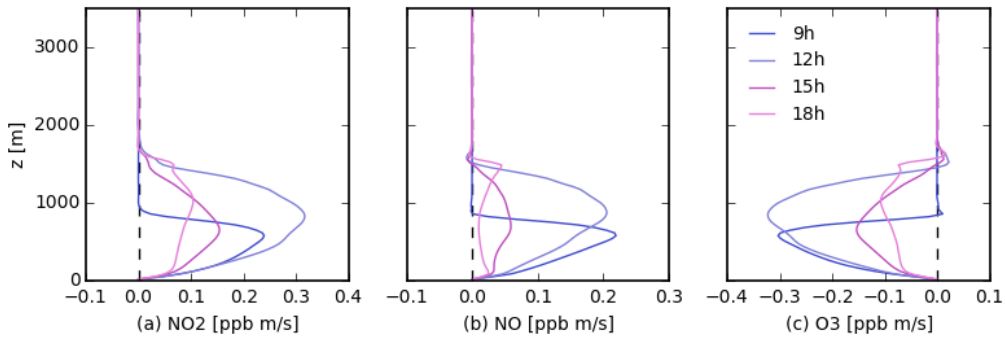

Figure 3.6: Evolution of 10-minute slab averaged resolved vertical flux profile of control case C0. (a) NO_2 flux; (b) NO flux; (c) O_3 flux.

3.1.1 Sensitivity to background ozone concentration

As mentioned at the beginning of this section, the background ozone concentration is important to the NO_x concentration fields. The emission of NO from combustion processes at ground level may get oxidized by tropospheric ozone quickly. The purpose of this section is to explore the dependency of NO_2 concentration to background ozone level. In this experiment, the interface model CLASS rather than DALES is used to run the simulation, considering CLASS is much simpler than DALES to control the chemical equilibrium and provides similar outputs to DALES. Moreover, the $NO_x - O_3$ system depends on the radiation. This diurnal cycle pattern should be avoided in this sensitivity study, thus a long time series simulation is necessary. Compared with DALES, CLASS provides instantaneous outputs at very low computational cost.

The CLASS simulation starts from local time 6 a.m. of 26th June, 2012, and performs for 10 consecutive days. The wind and large scale forcing terms are set to be zero. The photolysis rate j depends on radiation and the second order reaction rate k keep fixed for each case. Table. 3.2 lists all the cases run by CLASS, including a control case CC0, a control case CC1

with $O3$ surface emission, another three cases based on CC0 with higher background ozone level (case HO3), lower background ozone level (case LO3) and entrainment ozone from the upper atmosphere (case EO3). All parameters for control experiment CC0 are presented in Table. 3.3 and Figure. 3.7.

Table 3.2: Sensitivity study of background ozone concentration, consisting of control case without NO surface emission CC0, control case with O_3 surface emission SO3, case with high O_3 concentration, and case with O_3 entrainment from the upper part of the atmosphere.

Case	O_3 [ppb]	ΔO_3 [ppb]	$\overline{w'c'_{NO}}$ [$ppbms^{-1}$]	Description
CC0	20	0	0.0	Control case of CLASS, without surface NO emission, equilibrium case
SO3	20	0	0.1	Surface emission of ozone
HO3	30	0	0.0	High background ozone concentration
LO3	10	0	0.0	Low background ozone concentration
EO3	20	10	0.0	Entrainment of ozone from upper atmosphere

Table 3.3: Parameters in CLASS for control case (CC0).

Parameter	Value	Unit	Description
DOY	178	-	Day of the year
t	240	[h]	Simulation time
Time	4	[h]	Start time (UTC, local time 6 a.m.)
Latitude	51.91	[$\circ$]	Latitude of Rotterdam center
Longitude	4.48	[$\circ$]	Longitude of Rotterdam center
h_0	388.85	[m]	Initial boundary layer height
θ_0	285.764	[K]	Initial liquid water potential temperature in mixed layer
$\delta\theta_0$	2	[K]	Initial temperature jump at boundary layer
γ_θ	0.006	[Km^{-3}]	Potential temperature lapse rate at free atmosphere
$\overline{w'\theta'}$	0.0629	[Kms^{-1}]	Surface heat flux
q_0	7.7	[gkg^{-1}]	Initial total water specific humidity in the mixed layer
δq_0	-1.5	[gkg^{-1}]	Initial specific humidity jump at boundary layer
γ_q	0	[$gkg^{-1}m^{-1}$]	Specific humidity lapse rate at free atmosphere
$\overline{w'q'}$	0.0121	[$gkg^{-1}ms^{-1}$]	Surface moisture flux
$\overline{w'c'_{NO}}$	0.0	[$ppbms^{-1}$]	Surface emission of NO

As shown in Figure. 3.8, the daily cycle of NO_2 that decreases at first followed by an increase, responds to the solar radiation diurnal cycle. If there is no surface emission, in

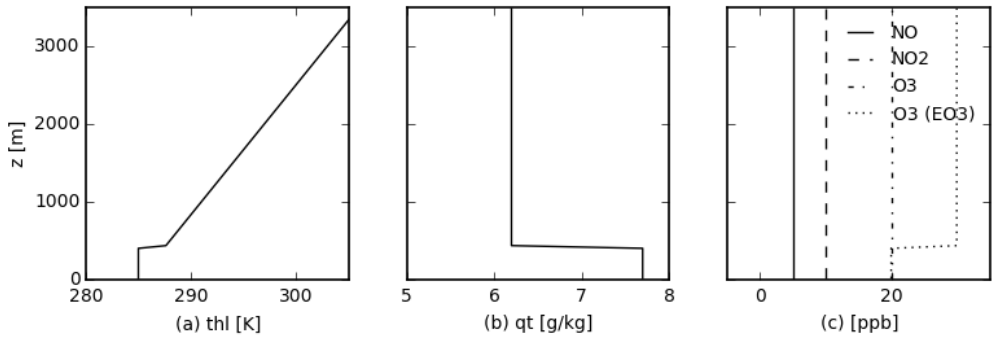

Figure 3.7: The initial profiles of (a) liquid water potential temperature (θ_l); (b) total water specific humidity (q_t); (c) chemical reactants concentration of NO_x and O_3.

CLASS, the $NO_x - O_3$ system is balanced and the concentration fields always return to the initial level. The periodic horizontal line in the figure means the photolysis reaction is suspended during nighttime where there is no radiation. Due to negligible amount of NO compared to O_3, the equilibrium concentration of NO reaches to zero. Thus, the NO_x is mainly in form of NO_2 (Figure.3.9). By changing the background values of ozone, the variation in NO_2 concentration can be studied. If raising O_3 amount in the mixed layer (case HO3), which involves more NO in the thermal reaction, and generate more NO_2. Consequently, the fraction of NO_2 in total NO_x during the daytime is significant at level of 70% (Figure. 3.9). Including a surface emission or an entrainment from upper free atmosphere of O_3 (case SO3 or EO3, Figure. 3.7 (c)) has a similar influence on NO_x concentration. But the case with surface emission disrupts the chemical equilibrium. The increasing O_3 leads to a rising in NO_2 production. At the end of the simulation, the NO_2 fraction is at level of 80%. Contrary, the lower background ozone level has an opposite effect that the NO is dominating form of the NO_x during the daytime.

3.1.2 Sensitivity to reaction rate coefficients

According to Equation. 3.1, if keep the background ozone level constant, the ratio between j and k matters NO_2 fraction in total NO_x. The reaction rate coefficients usually are determined by experiment (Appendix. C.1). Depending on the experimental approaches and conditions, the coefficients vary significantly. To be consistent with other studies based on DALES, the reaction rate coefficients used in this research are the default values in DALES [de Arellano et al.(2011)]. Therefore, the different values of reaction rate coefficients are not part of this research. Instead, the effects of the radiation and thermal correction for reaction rate coefficients would be explored. This section still uses C0 as control case, where both radiation and temperature correction are applied. Here, pairs of the first order (j) and second order rate coefficients k) are listed in Table. 3.4. The radiation and temperature correction of reaction rate coefficients as function of solar zenith angle (χ_0) and temperature are presented in Figure. 3.10, respectively.

The influence of radiation correction is significant in the boundary layer reflected by the

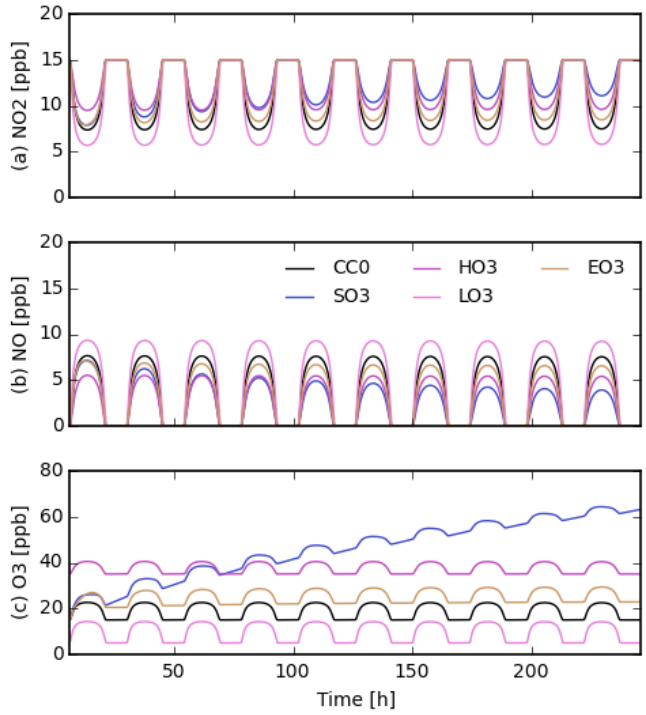

Figure 3.8: Evolution of concentration fields of CLASS simulation. (a) NO_2 concentration; (b) NO concentration; (c) O_3 concentration.

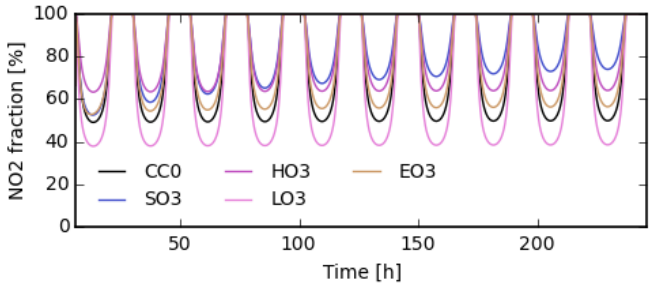

Figure 3.9: Evolution of NO_2 fraction of CLASS simulation.

comparison between case C0 and TD. The control case C0 generates less NO and O_3 because the photolysis rate of NO_2 is low (Figure. 3.11). On contrary, temperature dependent case TD enhances the NO and O_3 (Figure. 3.12) dramatically. The correction for temperature is considerable (Figure. 3.10 (b)), thus as shown in Figure. 3.3 (b) and 3.4 (a), there is barely NO left due to the fast thermal reaction with O_3 (Figure. 3.12).

As shown in Figure. 3.13 (a), without radiation correction, the NO_2 fraction in total NO_x reduces by approximately 20%. However, without the temperature correction, the NO_x is almost in form of NO_2 (dotted line, hardly can be seen). Conclusively, the correction for reaction rate coefficients is crucial to obtain reasonable outputs. The shape functions in all cases are similar, except that in case RD the NO_2 tends to be slightly higher than others in

Table 3.4: Sensitivity study to reaction rate coefficients, consisting of control case with cloud and temperature correction CL, case with only radiation correction RD and case with only temperature correction TD. The reaction rate coefficients are referred to [1] [de Arellano et al.(2011)];[2] [Schofield(1967)]; [3] [Ouwersloot et al.(2011)], where the original value is $1.67 \times 10^{-2} \times e^{-0.575}$, which is approximately equal to 9.40×10^{-3}.

Case	j [s^{-1}]	k[$cm^3 molec^{-1} s^{-1}$]	Description
C0	$1.67 \times 10^{-2} \times e^{\frac{-0.575}{\cos(\chi_0)}}$[1]	$3.00 \times 10^{-12} \times e^{\frac{-1500}{T}}$[1]	Correction for photolysis and temperature reaction
RD	$1.67 \times 10^{-2} \times e^{\frac{-0.575}{\cos(\chi_0)}}$	3.00×10^{-12}[2]	Only has correction for photolysis
TD	9.40×10^{-3}[3]	$3.00 \times 10^{-12} \times e^{\frac{-1500}{T}}$	Only has correction for thermal reaction

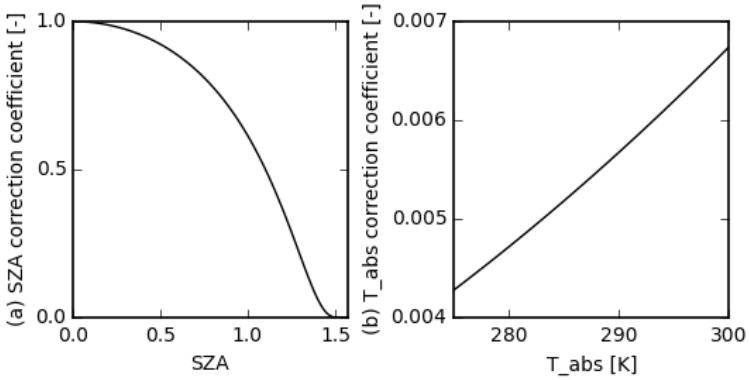

Figure 3.10: Correction for reaction rate coefficients. (a) cloud dependent correction as function of solar zenith angle (SZA); (b) temperature dependent correction as function of absolute temperature.

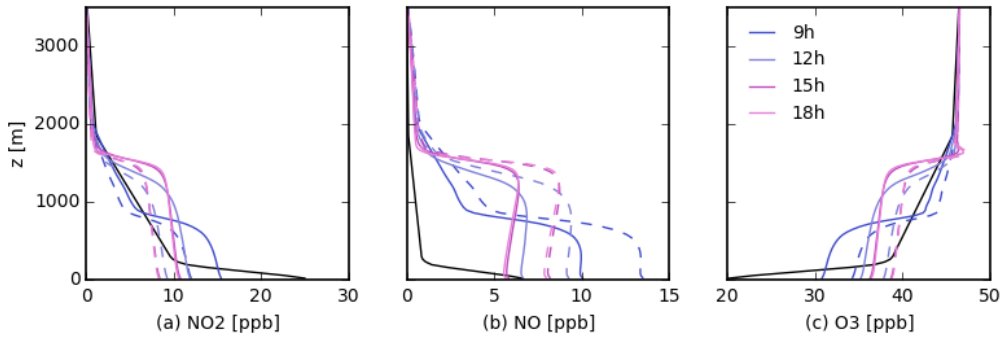

Figure 3.11: Evolution of 10-minute slab averaged concentration fields of control case C0 (continuous line) and case with temperature correction TD (dashed line). (a) NO_2 concentration; (b) NO concentration; (c) O_3 concentration. The black line indicates the initial profile.

the boundary layer due to the rapid reaction of NO and O_3.

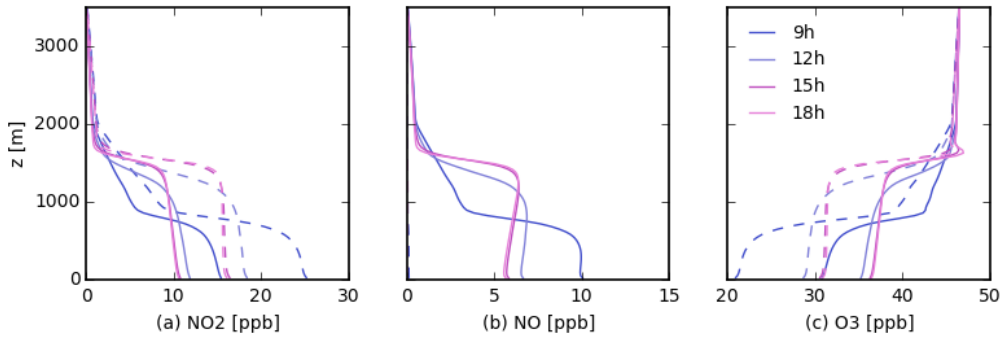

Figure 3.12: Evolution of 10-minute slab averaged concentration fields of control case C0 (continuous line) and case with radiation correction RD (dashed line). (a) NO_2 concentration; (b) NO concentration; (c) O_3 concentration. The black line indicates the initial profile.

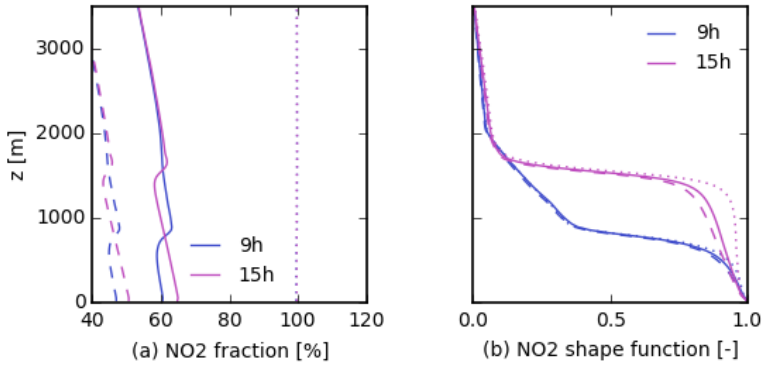

Figure 3.13: Evolution of 10-minute slab averaged concentration fields of quantities of control case C0 (continuous line), case with temperature correction TD (dashed line) and case with radiation correction RD (dotted line). (a) NO_2 fraction; (b) NO_2 shape function.

3.1.3 Sensitivity to clouds

The clouds is always a parameter of interest in atmospheric research. The presence of clouds makes satellite observation problematic by blocking the satellite signal to ground. Contrary, the ground-based remote sensing devices (e.g. MAX-DOAS) can only detect NO_2 columns below the clouds. Thus, a model simulation is necessary to represent the entire cloud influenced concentration fields. As a numerical tool, DALES is powerful enough to study the NO_2 profile shape in the presence of the clouds.

The clouds exerts impact on concentration fields in two ways in general. Chemically, the clouds disturb the reaction rate coefficients as described previously (Equation. 2.11 to 2.14); physically, the transport inside the clouds influences the vertical distribution of concentration field [de Arellano et al.(2005)]. In this section, there are two cases performed (Table. 3.5), the control case C0, that is slightly cloudy during the simulation, and a case under a more cloudy sky CL by setting $wqsurf$ to a large value. This value is calculated by averaging the surface moisture flux from 6 a.m. to 18 p.m.. On the one hand it takes consideration of larger values at noon, on the other hand it avoids extreme cases.

The evolution liquid water specific humidity (q_l) of control case C0 and cloudy case CL is in Figure. 3.14. The clouds formation of case CL starts earlier around 9 a.m., and evolves heavier with time.

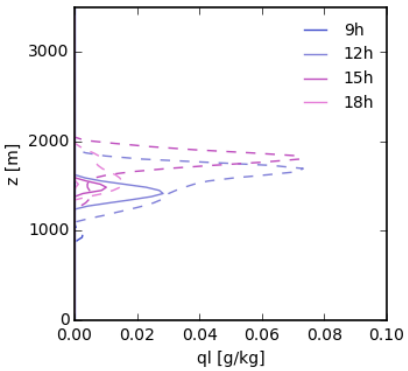

Figure 3.14: Evolution of 10-minute slab averaged liquid water specific humidity (q_l) of control case C0 (continuous line) and cloudy case CL (dashed line).

Reflected by the concentration fields of case C0 (continuous line) and CL (dashed line), the enhancement of vertical transport in cloud layer is obvious (Figure. 3.15). At initial phase of the simulation, the profile shapes of two cases are similar. Since the onset of clouds, the compounds are vertically redistributed to the upper part of the atmosphere (Figure. 3.15 and 3.16 (b)).

The clouds, on the other hand, perturbs the reaction rate coefficients. According to the clouds correction for the reaction rate coefficients as described in previous section (Equation. 2.12 to 2.14), the photolysis reaction above the clouds is enhanced by the reflected sunlight. Correspondingly, Figure. 3.15 (a) shows the reduction of NO_2 by enhanced photolysis in the cloud layer. However, it is difficult to elaborate the cloud perturbation of reaction rate coefficients in the cloud and sub-cloud layer. Whether increase or decrease the photo-dissociation mainly depends on the amount of liquid water content.

As Figure. 3.15 (a) shows, in the boundary layer, the concentration is slightly lower in more cloudy case CL. The reason cloud be the redistribution of concentration fields driven by clouds overwhelms the impact of cloud perturbation on photolysis. Or more likely, the effect of perturbed photo-dissociation is smoothed by the spatial and temporal averaging. Hence,

Table 3.5: Sensitivity study to the clouds, consisting of control case C0 and a more cloudy case CL.

Case	$wqsurf$ $[gkg^{-1}ms^{-1}]$	Description
C0	0.0112	Control case, where there is less clouds form during simulation
CL	0.5918	Cloudy case. Using a larger surface moisture flux (the mean surface moisture flux from 6 a.m. to 18 p.m.) to generate heavy clouds.

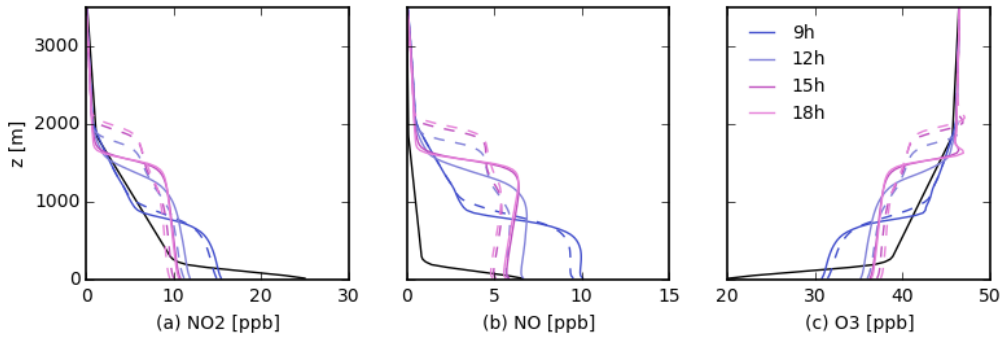

Figure 3.15: Evolution of 10-minute slab averaged concentration field profile of control case C0 (continuous line) and cloudy case CL (dashed line). (a) NO_2 concentration; (b) NO concentration; (c) O_3 concentration. The black line indicates the initial profile.

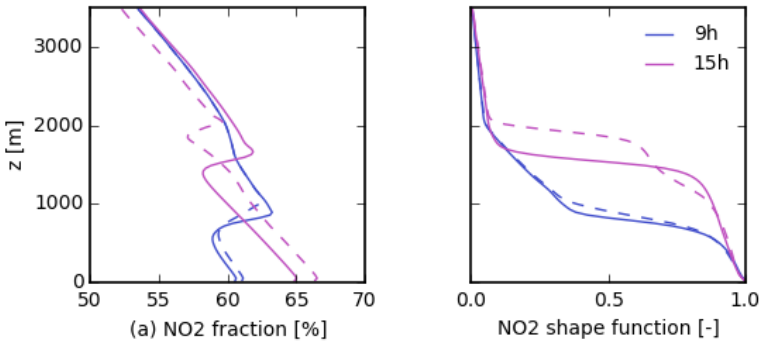

Figure 3.16: Evolution of 10-minute slab averaged quantities of control case C0 (continuous line) and cloudy case CL (dashed line). (a) NO_2 fraction; (b) NO_2 shape function.

here provides an instantaneous vertical cross section at 12 p.m of local time. Note that here the simulation is under more coarse resolution of 100 $m\times$ 100 $m\times$ 35 m, due to the processing limitation of personal computer. According to Figure. 3.17 (a), the NO_2 concentration field beneath the clouds is higher than the area without cloud and the concentration is more vertically distributed. Oppositely, the contour in clear sky case is more horizontally layered. In Figure. 3.17 (c) provides the difference between two cases. The largest difference up to 50% in the boundary layer, differing from the result of slab averaging.

3.1.4 Sensitivity to turbulent control

The turbulent control on concentration fields is a unique pattern in DALES, which is missing from LOTOS-EUROS. Generally, strong convection leads to more turbulence (high Reynolds number). Therefore, based on the case C0, a less turbulent case LT is simulated by setting no wind fields and large scaling forcing terms (Table. 3.6).

The time evolution of dynamics shows that case LT develops higher boundary layer and more liquid water content (Figure. 3.18, dashed line), and the clouds become heavier with time.

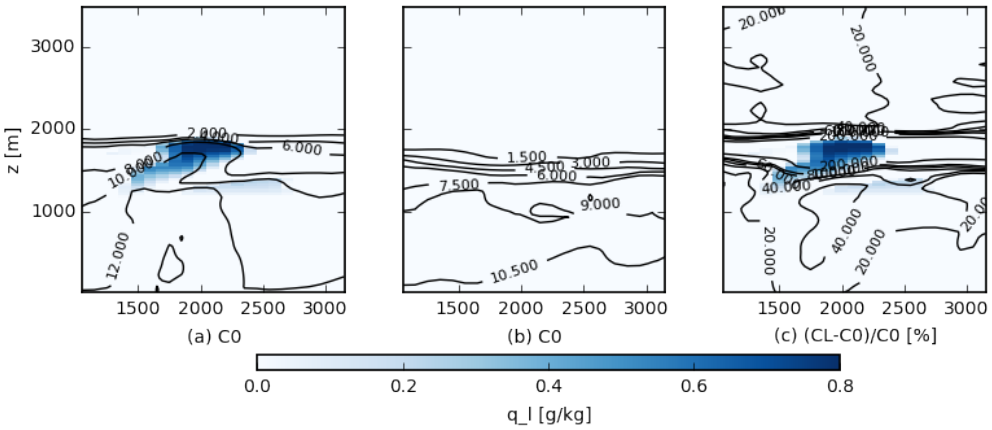

Figure 3.17: X-Z axis cross section at 12 p.m of local time. The shading indicates liquid water specific humidity (q_l); the contour presents the information about concentration fields. (a) control case C0; (b) cloudy case CL; (c) NO_2 concentration difference between case C0 and CL.

The turbulent control on concentration fields is quantified by the concept of segregation intensity (Equation. 3.2). At the beginning the I_s are similar to each other since no cloud exists. In the transition layer where the concentration gradients are large thus the I_s is significant (absolute value of 6%). With onset of clouds formation, the NO and O_3 are well-mixed by turbulence in the boundary layer (Figure. 3.19 (a)). But in the cloud layer, the species remain segregated because the clouds disrupts the spatial homogeneity of the concentration fields and leads to the large gradients of transports the reactants separately. The maximum (absolute value) I_s is only 1% of control case when the clouds becomes mature, while in less turbulence case, the maximum I_s is over 3%.

The influence of turbulence on NO_2 fraction and shape function is reflected by the clouds perturbation. According to Figure. 3.21 (a), due to the perturbation of clouds in less turbulent case LT is much stronger, the NO_2 fraction is larger in the sub-cloud layer compared with control case C0. On contrary, above the clouds, the NO_2 fraction is much larger in control case C0 due to lower photolysis rate. Reflected by the profile shape, the vertical transport in case LT is considerable at 15 p.m. when the clouds becomes mature.

Table 3.6: Sensitivity study to turbulent control, consisting of control case C0 and a less turbulent case LT.

Case	Wind profile	Large scale forcing	Description
C0	Yes	Yes	Control case, applying the initial wind profiles (u, v) and large scale forcing terms (ug, vg, $wfls$)
LT	No	No	Less turbulent, where wind profiles (u, v) and large scale forcing terms (ug, vg, $wfls$) are set to be zero

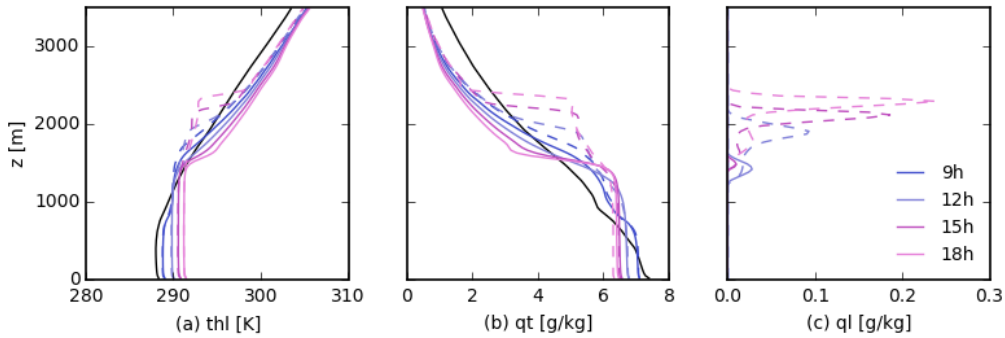

Figure 3.18: Evolution of 10-minute slab averaged dynamics of control case C0 (continuous line) and less turbulent case LT (dashed line). (a) liquid water potential temperature (θ_l); (b) total water specific humidity (q_t); (c) liquid water specific humidity (q_l). The black line indicates the initial profile.

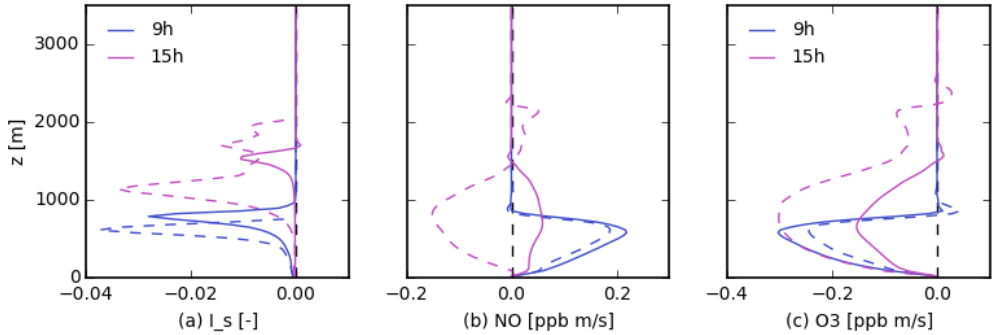

Figure 3.19: Evolution of 10-minute slab averaged quantities of control case C0 (continuous line) and less turbulent case LT (dashed line). (a) segregation intensity (I_s) of second order reaction; (b) NO flux; (c) O_3 flux.

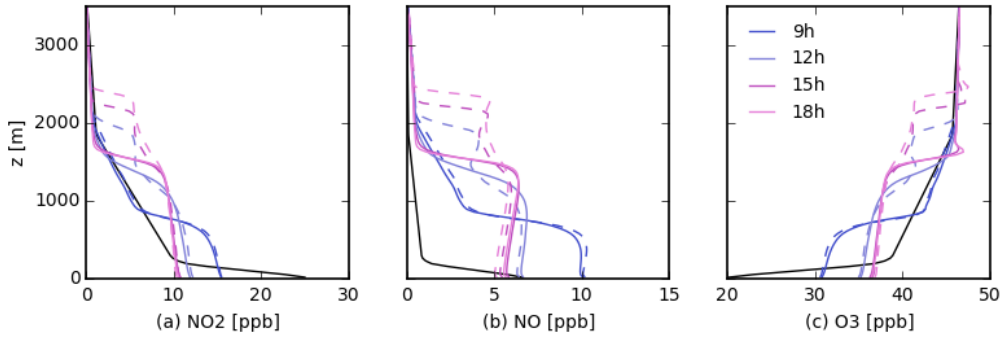

Figure 3.20: Evolution of 10-minute slab averaged concentration field profile of control case C0 (continuous line) and less turbulent case LT (dashed line). (a) NO_2 concentration; (b) NO concentration; (c) O_3 concentration. The black line indicates the initial profile.

3.2 Simulations over Rotterdam region

In the previous part, the sensitivity of NO_2 concentration field to chemistry and dynamics in DALES is performed, to explore the properties of DALES chemistry module. The background

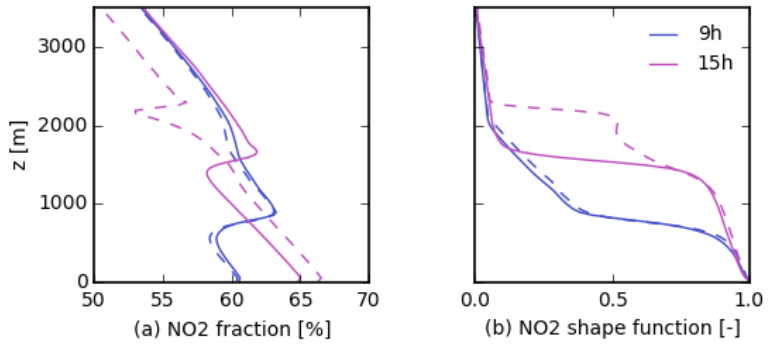

Figure 3.21: Evolution of 10-minute slab averaged quantities of control case C0 (continuous line) and less turbulent case LT (dashed line). (a)NO_2 faction; (b) NO_2 shape function.

ozone level and reaction rate coefficients collectively determine the concentration of NO_2. Meanwhile the clouds and turbulence impact the profile by redistributing the concentration field, which distinguishes DALES from LOTOS-EUROS. In the following sections, the simulation over Rotterdam region are performed and explained based on the properties of concentration field of DALES. The DALES simulation outcomes are further compared with LOTOS-EUROS, both in the vertical slab averaged profiles and horizontal spatial patterns. But firstly, to prove the capability of DALES, the simulated results are evaluated by satellite observational data.

To ensure that DALES simulations is comparable to LOTOS-EUROS simulation, the ECMWF driven meteorology should be used. But the due to the lack of large scale forcing terms and the unreasonable surface fluxes, the outputs simulated by ECMWF meteorology data are presented in Appendix B for reference. Here, in this section, the RACMO meteorological fields is in use. All the information of initial conditions for DALES are presented Figure. B.1, 3.23 and Table. 3.7. To compatible with LOTOS-EUROS, the time dependent large scale forcing and surface fluxes are applied. In addition, two resolutions are applied, the coarse one is 500 $m\times$ 500 $m\times$ 35 m, another one is 50 $m\times$ 50 $m\times$ 35 m. As show in Appendix A, for slab averaged quantities, the simulation based on fine resolution produces similar concentration fields as more coarse resolution simulation. Hereto, the coarse resolution is in use.

The development of dynamics for four cases are presented from Figure. 3.24 to 3.27. The development of the boundary layer in winter cases is not significant due to the small surface heat flux. The existence of liquid water content indicates the growth of the clouds. In case S1, the clouds is much denser than case S2, which is consistent with the local observation in Figure. 2.2.

The evolution of profiles are presented in Figure. 3.28 to 3.31. The profiles simulated by DALES are quite consistent with that of LOTOS-EUROS. Although the dense clouds form in two summer cases, the influences of clouds on profiles can hardly be detected. It reflects the LOTOS-EUROS control on DALES concentration is dominating, which will be explained in

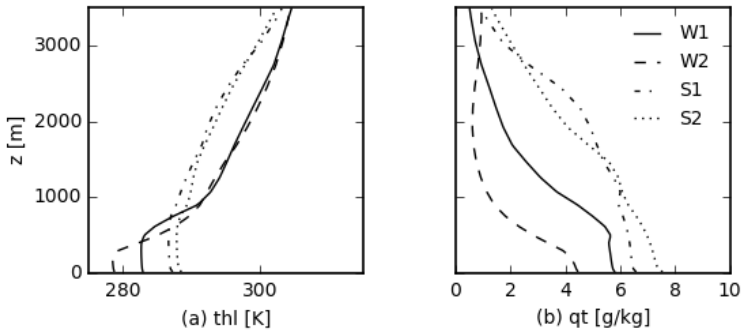

Figure 3.22: Initial profiles of ECMWF for four cases over Rotterdam region of (a) liquid water potential temperature (θ_l); (b) total water specific humidity (q_t).

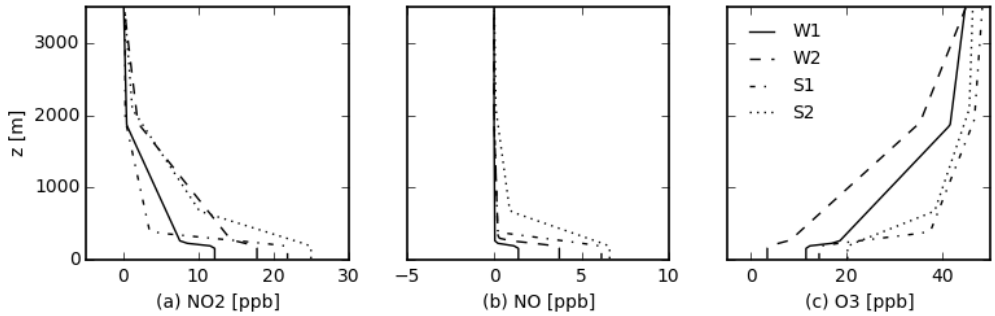

Figure 3.23: Initial profiles of four cases over Rotterdam region of (a) NO_2 mixing ratio; (b) NO mixing ratio and (c) $O3$ mixing ratio.

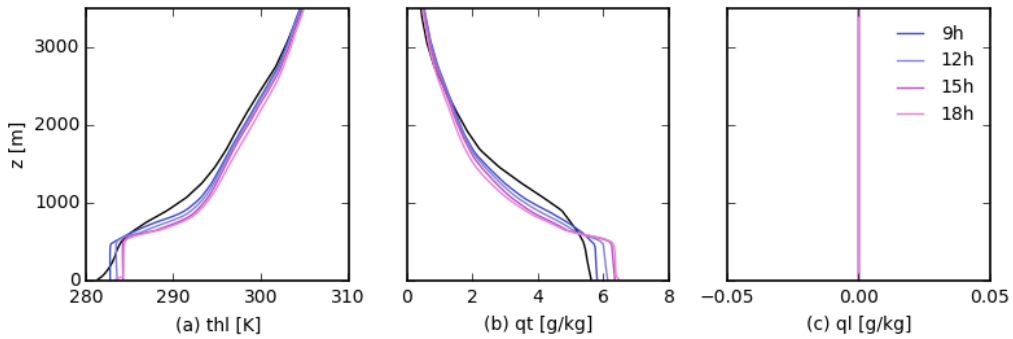

Figure 3.24: Evolution of 10-minute slab averaged dynamics for case W1. (a) liquid water potential temperature (θ_l); (b) total water specific humidity (q_t); (c) liquid water specific humidity (q_l). The black line indicates the initial profile.

Appendix B. The difference at beginning is always more considerable compared with the end of the simulation. Under the summer cases, the NO surface concentration simulated by DALES is halved, which is the most considerable discrepancy in profiles.

Table 3.7: Parameters in DALES for each case, consisting of a winter case at weekend W1, a winter case in week day W2, a summer case at weekend S1 and a summer case in week day S2. The reaction rate coefficients are referred to [1] [Schaap et al.(2005a)]. Here the meteorological information is from RACMO.

Parameter	Unit	W1	W2	S1	S2
Date	-	20111112 (SAT)	20111116 (WED)	20120602 (SAT)	20120626 (TUE)
xday	-	316	320	154	178
xtime	[h]	5	5	4	4
thls	$[K]$	276.721	272.957	282.546	285.746
ps	$[Pa]$	102607.0	102095.0	101898.0	102118.0
$\overline{w'\theta'}$	$[Kms^{-1}]$	-0.0185	-0.0196	0.0186	0.0147
$\overline{w'q'}$	$[gkg^{-1}ms^{-1}]$	-0.0002	-0.0004	0.0095	0.0112
runtime	$[s]$	43200			
itot	-	40			
jtot	-	30			
xsize	$[m]$	20000			
ysize	$[m]$	15000			
kmax	-	100			
xlat	$[\circ]$	51.91			
xlon	$[\circ]$	4.48			
j	$[s^{-1}]$	$1.45 \times 10^{-2} \times e^{\frac{-0.54}{\cos(SZA)}}$[1]			
k	$[cm^3 molec^{-1} s^{-1}]$	$2.00 \times 10^{-12} \times e^{\frac{-1400}{T}}$[1]			
lcloudKconst	-	false			

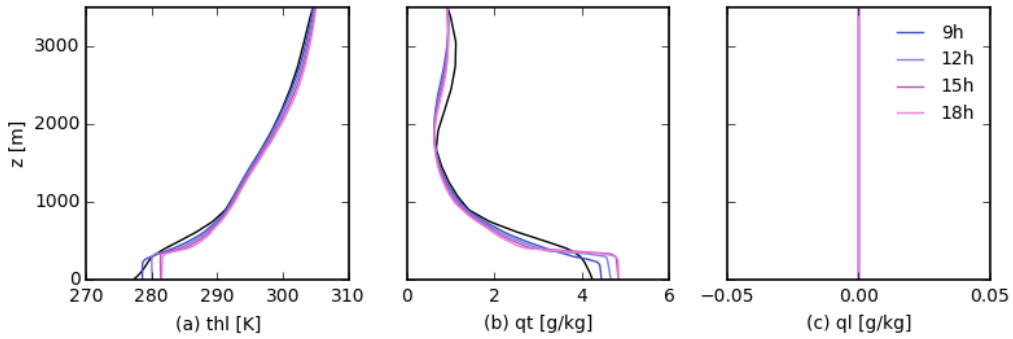

Figure 3.25: Evolution of 10-minute slab averaged dynamics for case W2.(a) liquid water potential temperature (θ_l); (b) total water specific humidity (q_t); (c) liquid water specific humidity (q_l). The black line indicates the initial profile.

3.2.1 Evaluation of simulations with satellite observations

To evaluate the simulated concentration fields, the observational data of satellite is employed. Here in this thesis is the Ozone Monitoring Instrument (OMI). As mentioned in Section 2.1, the data product is DOMINO (Dutch OMI NO_2 data). The tropospheric NO_2 slant column density (N^S) is measured, at local equator crossing time between 13 p.m. and 14 p.m.. The measured tropospheric N^S is further converted into tropospheric vertical column density

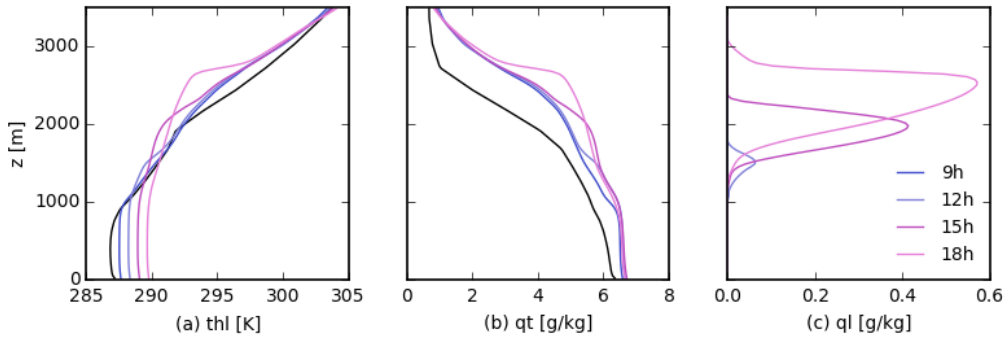

Figure 3.26: Evolution of 10-minute slab averaged dynamics for case S1.(a) liquid water potential temperature (θ_l); (b) total water specific humidity (q_t); (c) liquid water specific humidity (q_l).The simulation driven by RACMO leads to cloud formation. The black line indicates the initial profile.

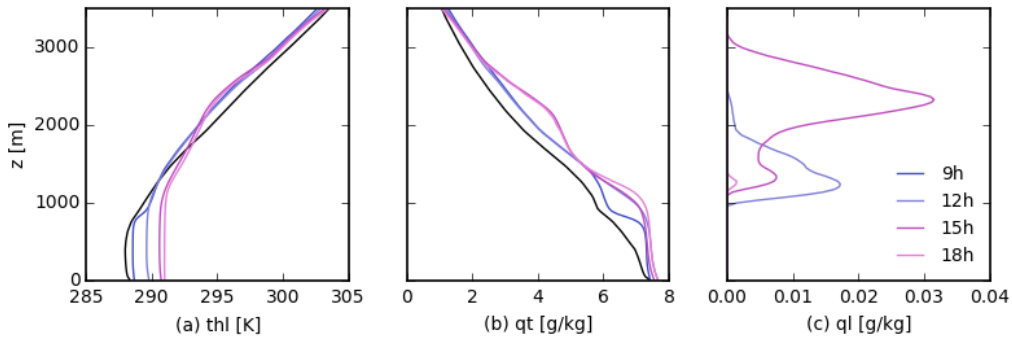

Figure 3.27: Evolution of 10-minute slab averaged dynamics for case S2.(a) liquid water potential temperature (θ_l); (b) total water specific humidity (q_t); (c) liquid water specific humidity (q_l). The simulation driven by RACMO leads to cloud formation. The black line indicates the initial profile.

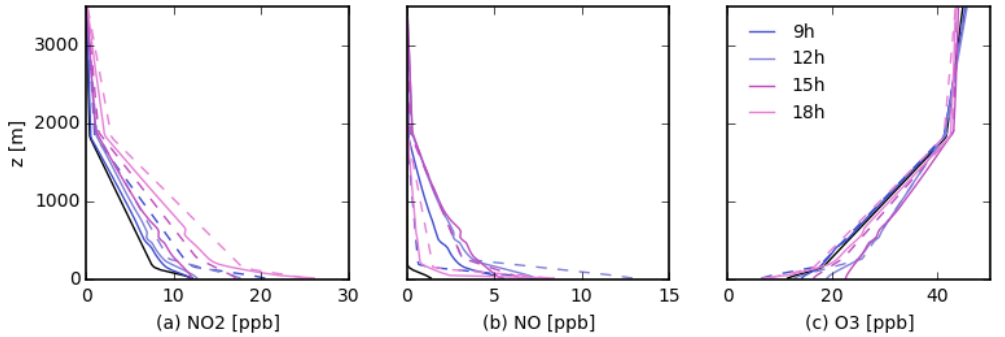

Figure 3.28: Evolution of 10-minute slab averaged concentration field profile of DALES (continuous line) and LOTOS-EUROS (dashed line) inputs for case W1. (a) NO_2 concentration; (b) NO concentration; (c) O_3 concentration. The black line indicates the initial profile.

(N^V) by considering the simulated tropospheric air mass factor (AMF) by chemistry trasport model TM4 (Equation. C.19).

The observational data is obtained under certain conditions that affected by meteorology, surface and measuring geometry, etc. These influences are collectively described by height

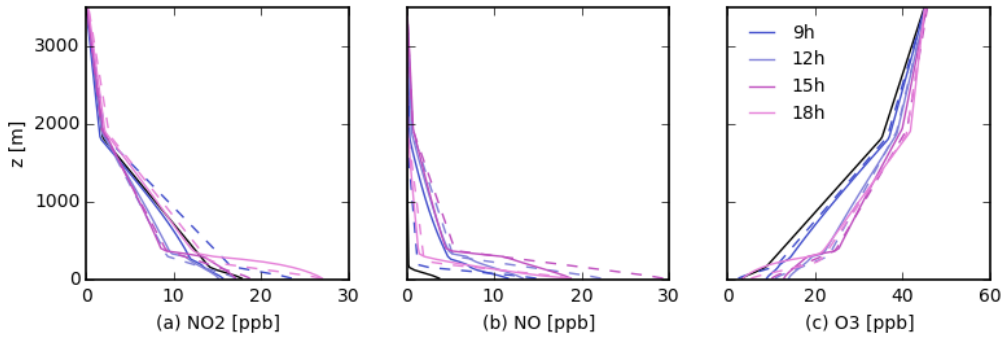

Figure 3.29: Evolution of 10-minute slab averaged concentration field profile of DALES (continuous line) and LOTOS-EUROS (dashed line) inputs for case W2. (a) NO_2 concentration; (b) NO concentration; (c) O_3 concentration. The black line indicates the initial profile.

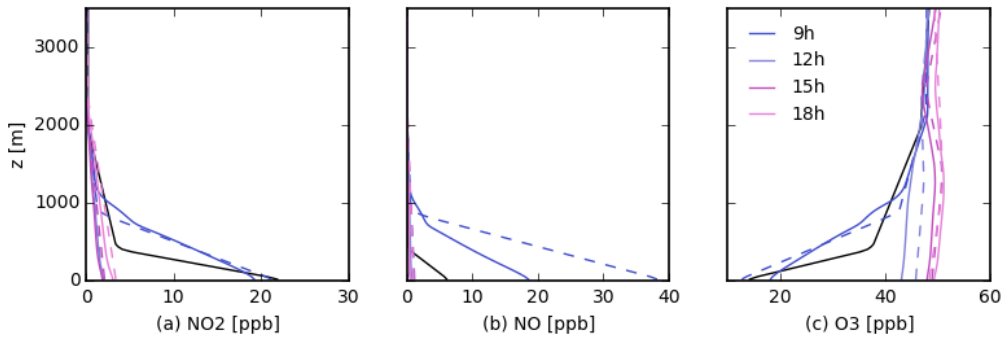

Figure 3.30: Evolution of 10-minute slab averaged concentration field profile of DALES (continuous line) and LOTOS-EUROS (dashed line) inputs for case S1. (a) NO_2 concentration; (b) NO concentration; (c) O_3 concentration. The black line indicates the initial profile.

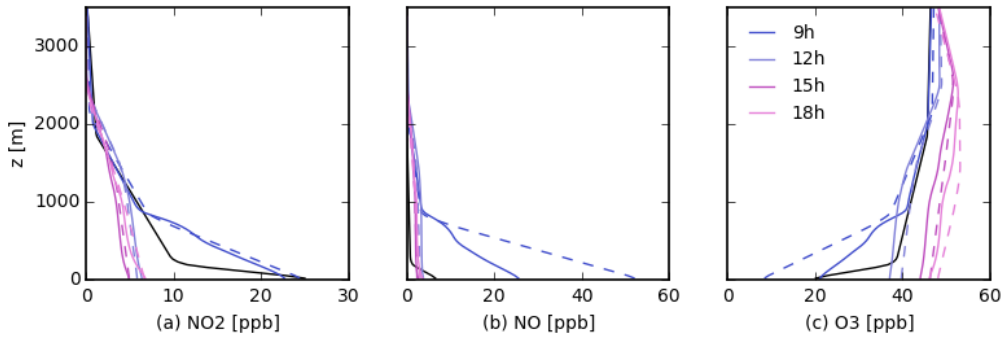

Figure 3.31: Evolution of 10-minute slab averaged concentration field profile of DALES (continuous line) and LOTOS-EUROS (dashed line) inputs for case S2.(a) NO_2 concentration; (b) NO concentration; (c) O_3 concentration. The black line indicates the initial profile.

dependent measurement sensitivity or height dependent air mass factor (box AMF). This sensitivity ensures the simulated column density is compatible to the observed under the same measuring conditions. One of the method is involving the concept of averaging kernel (AK, Equation. 3.3). AK is determined by dividing the box AMF by the total air mass factor

(AMF),

$$AK = \frac{BAMF_i}{AMF} \tag{3.3}$$

, where i is the specific atmospheric layer. AK provides information about the retrieved vertical column density (N^V) variation with absorber concentration at a certain height. By multiplying the trace gas profile of simulations, the direct comparison with satellite observations is possible [Burrows et al.(2011)] [Boersma et al.(2011)],

$$N_s^V = \sum_{i=0}^{TOA} AK_i \cdot N_i^V \tag{3.4}$$

, where N_s^V indicates the N^V of the simulated dataset that measured under the same condition of observations.

Figure. 3.32 provides the AK accompanying with DOMINO data product for each selected days. Under all situations, the surface sensitivity is attenuated due to various reasons, such as surface condition or cloud or aerosol layer. In the upper part of the atmosphere, the two winter cases show considerable AMF due to the viewing zenith angles are much larger than that in summer cases, which can reflected by the ground pixel size (Figure. 2.1). On the other hand, the two summer cases present stable increasing sensitivity with height.

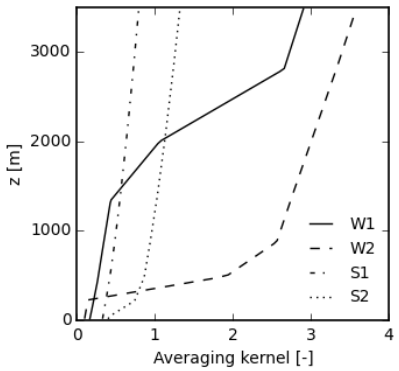

Figure 3.32: Averaging kernel (AK) from Ozone Monitoring Instrument (OMI) for each selected day.

The comparison with satellite observation is listed in the Table. 3.8. The uncertainty in winter cases is much larger. The main reason is the viewing zenith angles (VZA) in summer cases are smaller, meaning that the light path in the atmosphere is shorter, therefore less uncertainties. Both simulations behave well and lead to the result of the same magnitude as OMI data, and overall the DALES slightly surpasses LOTOS-EUROS, except for case W1. However, among all the cases, the relative difference between simulations and observation of case W1 is the smallest, for LOTOS-EUROS and DALES, the difference compared to OMI are 4.34% and -25.08%, respectively. Under other cases, though the discrepancy is considerable, the majority of the simulated result falls in range of 95% confidence interval (2 standard

deviations). Conclusively, both numerical models provide reliable results, and generally DALES behaves slightly better than LOTOS-EUROS in consistency with observations.

Table 3.8: Comparison of vertical column density (N^V, [$1 \times 10^{16} molec cm^2$]) among satellite observation and simulations.

Case	W1	W2	S1	S2
DALES	1.2456	5.8441	0.1827	1.5213
LOTOS-EUROS	1.7349	6.5394	0.2475	1.7156
OMI	1.6627	4.0789	0.7669	0.7659
OMI std	3.5254	4.6687	0.5254	0.6245

3.2.2 Comparison with LOTOS-EUROS

In previous section, the absolute concentration fields of DALES and LOTOS-EUROS are evaluated by OMI satellite observations. In general, DALES has higher consistency with measurements. But the total column density can not provide the information about the vertical distribution of air pollutants. In addition, the spatial variation is buries by slab averaging. In this part, thus, by comparing of vertical profiles and horizontal spatial patterns between DALES and LOTOS-EUROS, the potential benefits of DALES are explored.

Figure. 3.33 to 3.36 present the comparison between DALES and LOTOS-EUROS simulations of four cases over Rotterdam region. Overall speaking, the DALES show relatively high consistency with LOTOS-EUROS. The NO_2 fraction at ground level is relatively small due to the large amount of NO emission. The difference in winter days is constant with height, while in the summer days the difference is maximum in the boundary layer. Referring to Figure. 3.30 (b) and 3.31 (b), the NO near surface in DALES is underestimated. The maximum difference an up to 20% in case W1. The NO_2 fraction is minimum during 12 p.m. to 15 p.m., during which the photolysis rate is the highest.

If only considering the NO_2 profile, both numerical models highly agree with each other. The DALES simulated NO_2 shape functions are slightly higher than LOTOS-EUROS at the beginning of the simulation. During the latter half of the simulation, the DALES concentration field are more concentrated to surface. It cloud because the coarse vertical resolution of LOTOS-EUROS concentration fields that can hardly describe the small gradient with height (Figure. 3.30 (a) and 3.31 (a)).

The vertical distribution of concentration fields of DALES shows high consistency with LOTOS-EUROS. But the horizontal slab averaged quantities could weaken the spatial patterns. Consequently, the remaining section will study the spatial and temporal difference between the two numerical models. To concisely describe the horizontal concentration fields, two parameters are used, namely the surface concentration ($c(0)$) and total tropospheric vertical column density (N^V) integrated from the surface to the top of the atmosphere (here is the top of the model domain).

In Figure. 3.37 to 3.40, the black lines indicate the slab averaged $c(0)$ and N^V as function of time of DALES (continuous line) and LOTOS-EUROS (dashed line) simulation, respectively.

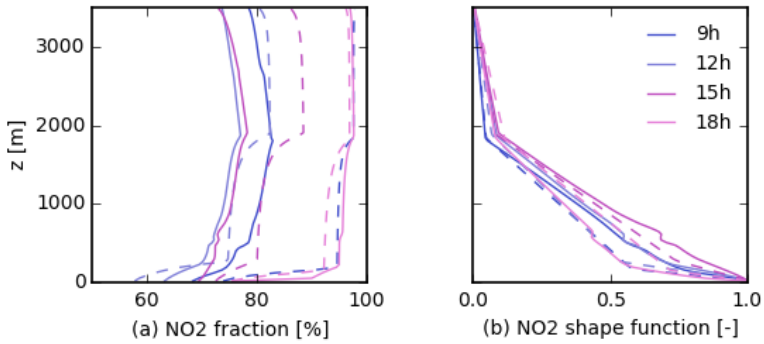

Figure 3.33: Evolution of 10-minute slab averaged concentration field profile of DALES (continuous line) and LOTOS-EUROS (dashed line) for case W1. (a) NO_2 fraction; (b) NO_2 shape function.

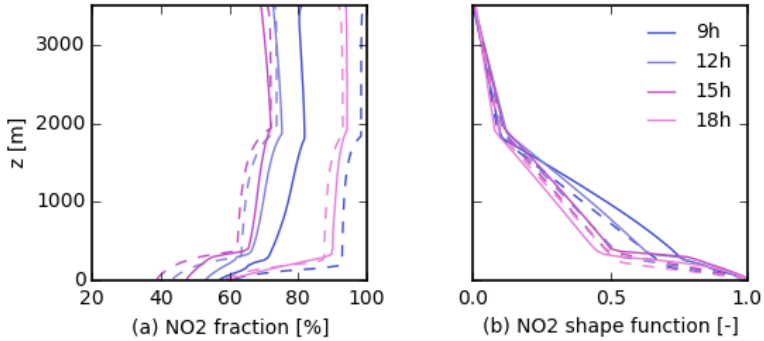

Figure 3.34: Evolution of 10-minute slab averaged concentration field profile of DALES (continuous line) and LOTOS-EUROS (dashed line) for case W2. (a) NO_2 fraction; (b) NO_2 shape function.

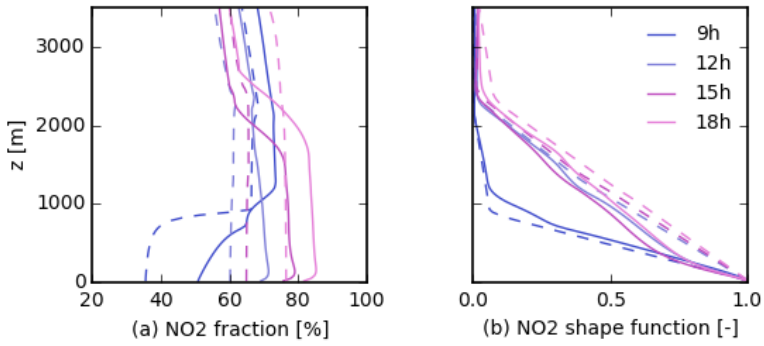

Figure 3.35: Evolution of 10-minute slab averaged concentration field profile of DALES (continuous line) and LOTOS-EUROS (dashed line) for case S1. (a) NO_2 fraction; (b) NO_2 shape function.

Generally, the $C(0)$ and N^V have similar trend, meaning the NO_2 is mainly distributed at the ground level, and the column density is largely controlled by this surface concentration. The NO_2 concentration in week days (case W2 and S2) are higher than that at weekend (case

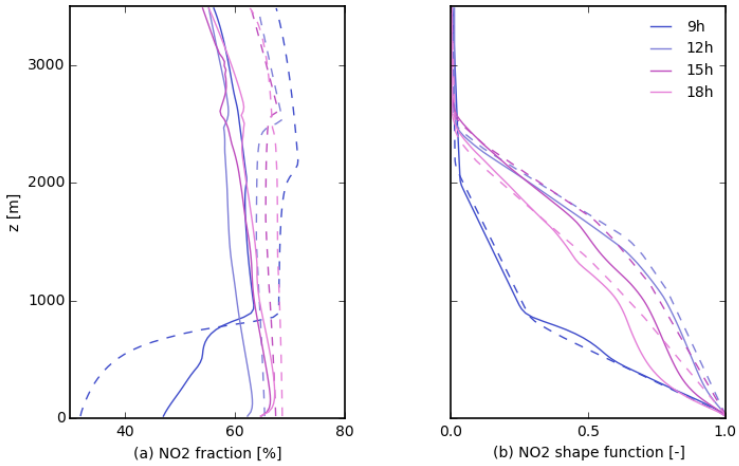

Figure 3.36: Evolution of 10-minute slab averaged concentration field profile of DALES (continuous line) and LOTOS-EUROS (dashed line) for case S2. (a) NO_2 fraction; (b) NO_2 shape function.

W1 and S1). Among all cases, the case W2 and S2 have the highest consistency between two models (Table. 3.9).

The NO_2 $c(0)$ and N^V during winter days show an increasing trend, but the trend for case W2 presents a clear diurnal cycle, with respect to the emission diurnal cycle Figure. 2.6 (c). The difference between DALES and LOTOS-EUROS in case W1 seems to be a systematic shift. For both $c(0)$ and N^V the time averaged difference is the highest among all cases (Table. 3.9). Compared with this, the gap is only significant at peak values of case W2, where the relative difference is up to approximately 40% (Figure. 3.42 (a)). This peak value is DALES is around 1 hour earlier than LOTOS-EUROS simulation.

In both summer cases, for parameter $c(0)$ and N^V there is a peak at around 8 a.m., followed by a decreasing trend. But there is a time delay of DALES simulation compared with LOTOS-EUROS. This delay causes significant relative difference (Figure. 3.43 (a) and 3.44 (a)). The time averaged difference is therefore enhanced by this delay (Table. 3.9).

The reason for the above differences cloud be collective influence of various factors. For case W1, the emission inventory could be the dominating reason for systematic offset. Because DALES only applies traffic emission that assimilated in URBIS, while LOTOS-EUROS uses MACC-III emission inventory that covers more categories of pollution sources. For the difference at peak of case W2 and the time delay in two summer days, the reason can be the reaction rate coefficients and the chemical mechanism, or dynamics parameter such as wind.

To study the horizontal spatial variability, totally five locations are selected that are sparsely distributed in the region of interest (ROI) as shown in Figure.3.45. Location 1, 2, 4 and 5 are at the four corner of the domain, which are near the highway with high emission, location 3 is at the center of the domain. Here need to mention, because the limited capability to restore and process the high resolution (50 $m\times$ 50 $m\times$ 35 m) outputs, only the spatial

information based on coarse resolution (500 $m\times$ 500 $m\times$ 35 m) simulation is in use. The compromising in resolution leads to that the potential benefits of DALES dynamics, such as turbulence, can not be studied. But even based on this coarse resolution, it is still much higher than LOTOS-EUROS resolution (0.0625 $^\circ\times$ 0.125 $^\circ$, approximately 7$km\times$ 9 km), and can show more spatial patterns.

Based on the Figure. 3.37 to 3.40, the local $c(0)$ and N^V trend of LOTOS-EUROS are more consistent with their corresponding slab averaged values (dashed line), while DALES presents more spatial variability. According to the relative difference presented in Figure. 3.41 to 3.44, for both model simulations, the difference at surface is slightly larger than N^V, indicating the vertical integrated concentration is less dependent on location. The difference in winter cases is much smaller, less than 40% and 20% for case W1 and W2, respectively. On contrary, although after 11 a.m. in summer cases, the absolute difference between each location and slab averaged concentration is negligible, the relative difference enlarges the spatial and temporal patterns. The difference of maximum $c(0)$ and N^V can reach 100% (Figure. 3.43 (a) and 3.43 (b)). Among all the situations, case W2 shows highest representativeness of the whole domain. Because the majority of relative difference is less than 20%, and the relative difference trend of most of locations are similar (Figure. 3.42).

In the following analysis, focus are put on the $c(0)$ only to see what is the main reason causes the deviation from the slab averaged concentration. In both winter cases, the overall spatial variation is not considerable, because the wind direction under this case is constant during the day, and according to Figure. 3.28 (a) and 3.29 (a) , the evolution of profile is not significant, reflecting that the LOTOS-EUROS boundary constraints does not varies much. But exceptions exist. For instance, in case W1, the concentration of location 1 is always higher than other locations (Figure. 3.37 (a)), this difference reaches maximum at 14 p.m.. The instantaneous $C(0)$ situation of case W1 at this time is presented in the Figure. 3.45. The reason behind this high value is because location 1 is always at the downwind of a high concentration boundary that controlled by LOTOS-EUROS. In case W2, only at 9 a.m. the majority of the locations show low values compared with slab averaging (Figure. 3.38 (a)). The instantaneous surface condition shows that at that moment the low concentration control the majority of the locations, only the area in adjacent to the boundary controlled by high concentration (Figure. 3.29).

The two summer cases, as mentioned before, show more spatial variability. In summer case S1, the maximum value at location 5 occurs latter than others (Figure. 3.39 (a)) because the it is at the downwind of a low concentration area (Figure. 3.47), while other locations either adjacent to, or at the downwind of a high concentration region. The location 1 in

Table 3.9: Absolute mean relative difference between DALES and LOTOS-EUROS, calculated by making difference between LOTOS-EUROS and DALES, the the difference is divided by DALES.

Case	W1	W2	S1	S2
Difference of $c(0)$	36.55%	16.43%	22.62%	16.18%
Difference of N^V	26.59%	13.43%	26.19%	13.50%

case S2 behaves significantly different from other locations after 12 p.m. (Figure. 3.40 (a)). According to Figure. 3.48 showing the surface concentration at 13 p.m. when the second peak occurs, location 1 is exactly at the emission point. This property is not reflected by another summer case S1 because the emission factor for case S2 is much higher than S1 (Figure. 2.6 (b)).

Summarily, evaluated by the observations, the DALES simulations are slightly better than the LOTOS-EUROS. In terms of vertical profiles, both the resolution and the meteorology have limited influence on DALES. The difference is at level of 10%. The strong constraint of concentration boundary condition from LOTOS-EUROS ensures the DALES simulated shape function are highly consistent with LOTOS-EUROS. The relatively larger discrepancy in NO_2 fraction attributes to the difference in NO concentration at the beginning of the simulation. In terms of horizontal properties, both the numerical models still show high consistency. Except for case W1, the difference is present as a systematic bias, other cases show time delay at the beginning of the simulation, but 12 p.m. onwards, both models show high consistency. The reasons cloud be the emission inventory, chemistry and dynamics scheme. The horizontal spatial property shows that compared with $c(0)$, the N^V shows higher representativeness of the whole domain for both simulations. The considerable spatial variability in DALES is due to the high resolution. The potential benefit of more complicated dynamics such as turbulence, should be put more effort to study in the future.

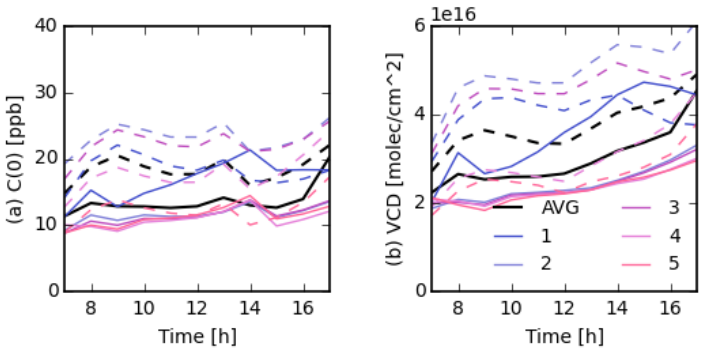

Figure 3.37: Evolution of 10-minute slab averaged concentration field profile of DALES (continuous line) and LOTOS-EUROS (dashed line) for case W1. (a) slab averaged and local $c(0)$; (b) slab averaged and local N^V.

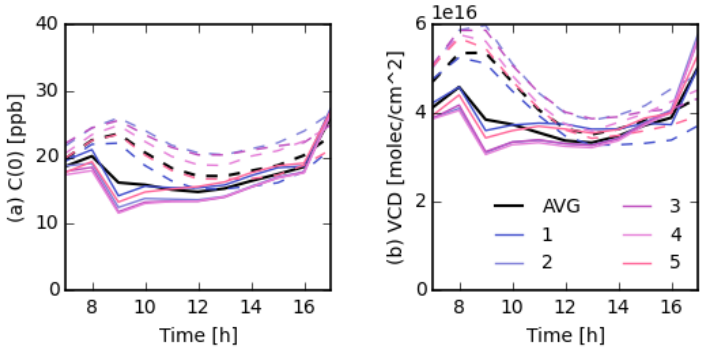

Figure 3.38: Evolution of 10-minute slab averaged concentration field profile of DALES (continuous line) and LOTOS-EUROS (dashed line) for case W2. (a) slab averaged and local $c(0)$; (b) slab averaged and local N^V.

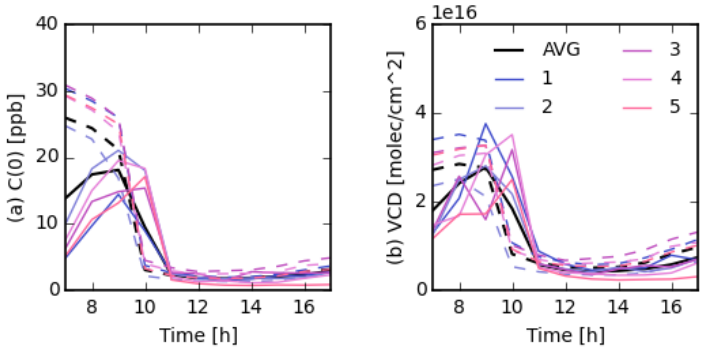

Figure 3.39: Evolution of 10-minute slab averaged concentration field profile of DALES (continuous line) and LOTOS-EUROS (dashed line) for case S1. (a) slab averaged and local $c(0)$; (b) slab averaged and local N^V.

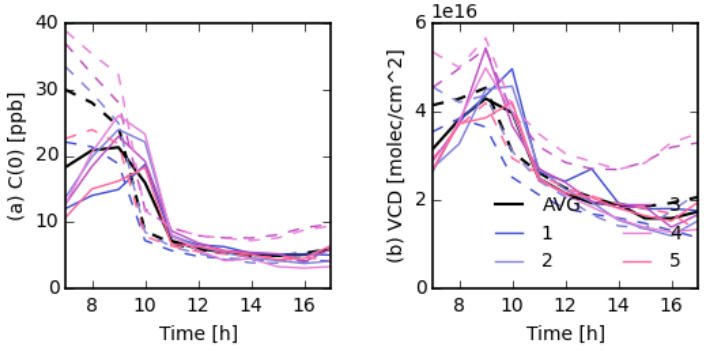

Figure 3.40: Evolution of 10-minute slab averaged concentration field profile of DALES (continuous line) and LOTOS-EUROS (dashed line) for case S2. (a) slab averaged and local $c(0)$; (b) slab averaged and local N^V.

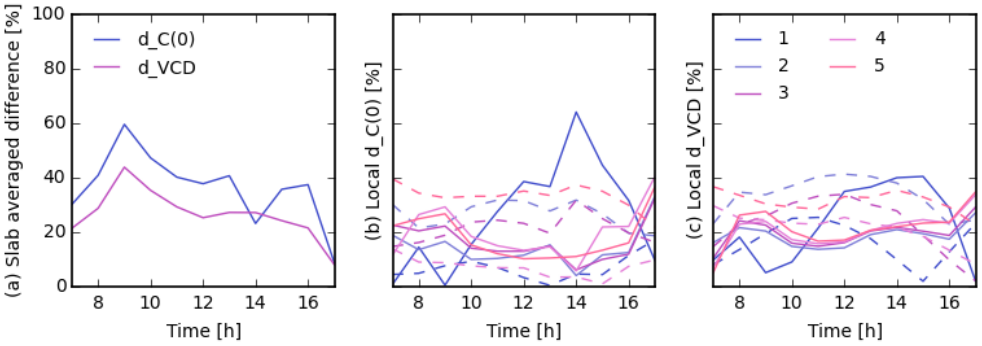

Figure 3.41: Absolute relative difference of DALES (continuous line) and LOTOS-EUROS (dashed line) for case W1. (a) NO_2 slab averaged $c(0)$ and N^V between DALES and LOTOS-EUROS. The ; (b) NO_2 $c(0)$ difference between local and slab averaged; (c) NO_2 N^V difference between local and slab averaged.

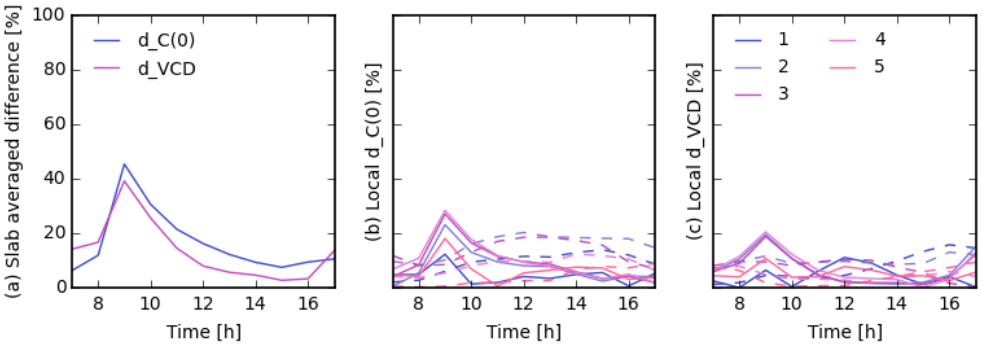

Figure 3.42: Absolute relative difference of DALES (continuous line) and LOTOS-EUROS (dashed line) for case W2. (a) NO_2 slab averaged $c(0)$ and N^V between DALES and LOTOS-EUROS; (b) NO_2 $c(0)$ difference between local and slab averaged; (c) NO_2 N^V difference between local and slab averaged.

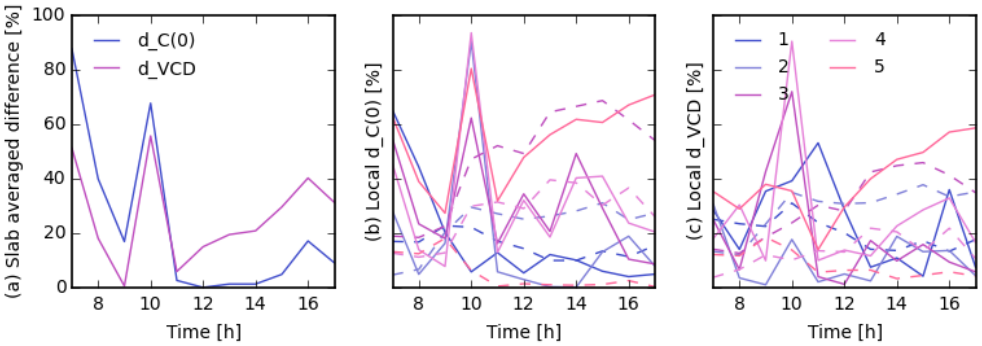

Figure 3.43: Absolute relative difference of DALES (continuous line) and LOTOS-EUROS (dashed line) for case S1. (a) NO_2 slab averaged $c(0)$ and N^V between DALES and LOTOS-EUROS; (b) NO_2 $c(0)$ difference between local and slab averaged; (c) NO_2 N^V difference between local and slab averaged.

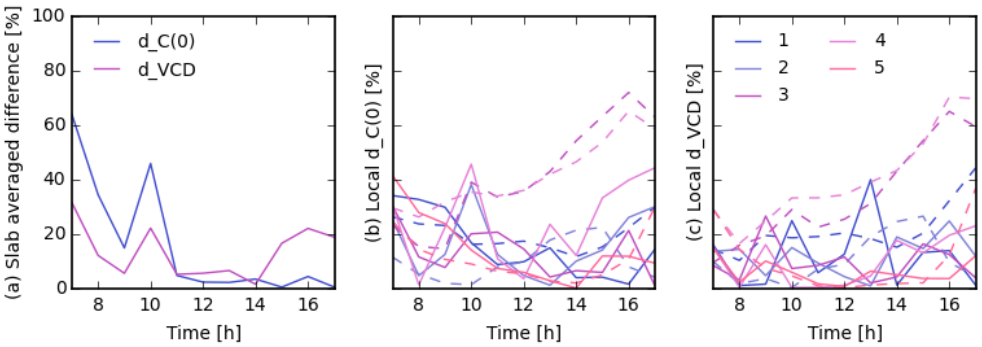

Figure 3.44: Absolute relative difference of DALES (continuous line) and LOTOS-EUROS (dashed line) for case S2. (a) NO_2 slab averaged $c(0)$ and N^V between DALES and LOTOS-EUROS; (b) NO_2 $c(0)$ difference between local and slab averaged; (c) NO_2 N^V difference between local and slab averaged.

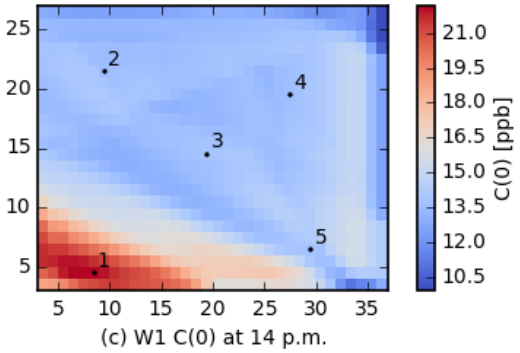

Figure 3.45: $c(0)$ at 14 p.m. of case W1. The wind direction is from south-east.

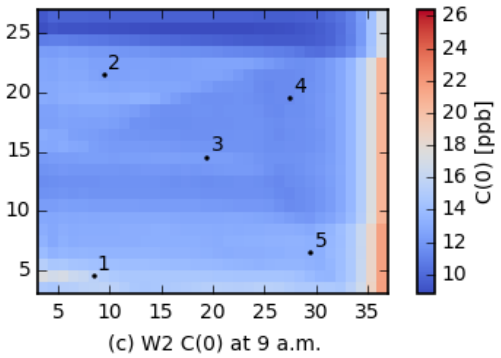

Figure 3.46: $c(0)$ at 9 a.m. of case W2. The wind direction is from east.

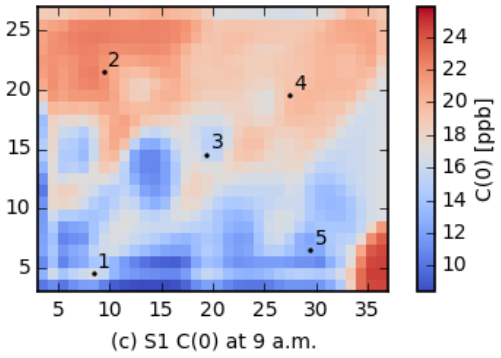

Figure 3.47: $c(0)$ at 9 a.m. of case S1. The wind direction is from north-east.

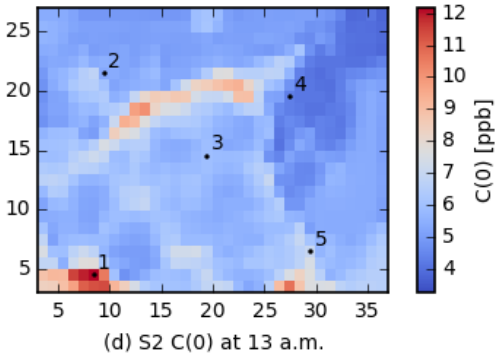

Figure 3.48: $c(0)$ at 13 p.m. of case S2. The wind direction is from north-east.

Chapter 4

Conclusion

A good knowledge in atmospheric compound profiles is the key in air quality research. It does not only provide the information about the vertical distribution of the specific composition, but also the surface concentration that affects human health mostly. The monitoring on profiles of air pollutants is essential. But in reality, the observations of profiles become challenging due to the meteorological conditions, practical and financial reasons. Another method to approach this issue is atmospheric numerical modeling. The development of computational ability enables to simulate the specific air pollutant profile with high precision. This precise vertical profile is not only essential for accurate vertical column retrievals based on passive UV/visible sensors, but also provides the information on the relation between the column and the surface concentration. Besides, the knowledge on spatial and temporal variability of trace gases vertical profile is important for interpretation of inter-comparisons among various observational datasets. This master thesis takes the first step to make a large eddy simulation based air quality model, initially focusing on nitrogen oxides, by nesting DALES into LOTOS-EUROS over Rotterdam.

4.1 Main conclusions

Before studying the impact of the LES-based air quality model on concentration and column over Rotterdam region, several academic experiments are performed to study the properties of the chemical module in DALES. The chemistry and atmospheric dynamics collectively determine and affect the concentration field of a specific species. In this thesis, focus is put on one of the most important urban pollutant, nitrogen dioxide (NO_2).

According to Equation. 3.1b, the fraction of NO_2 in NO_x is determined by the background ozone level and reaction rate coefficients. In Section 3.1.1, the sensitivity to the ozone concentration is determined with the CLASS model, which provides similar outputs as DALES instantaneously, and can easily simulate the equilibrium states of the chemistry and avoid the influence of diurnal radiation. The results show the increasing of the background O_3 concentration consumes more NO and generates more NO_2, raising the NO_2 percentage in total NO_x.

Three corrections for reaction rate coefficients are applied in the DALES chemistry module. They are correction for temperature, radiation and clouds (liquid water content). The former two corrections are studied in Section 3.1.2. The absence of the correction for temperature leads to unreasonable concentration fields, where no remaining NO due to the fast reaction rate. The radiation correction slows down the photo-dissociation and increases the NO_2 fraction by 20% when compared with simulation that without applying radiation correction. In spite the large difference in concentrations, the profile shape is barely affected by whether the correction for reaction rate coefficients is applied or not.

The correction for clouds is more complicated (Section 3.1.3). Theoretically, the photolysis above the clouds is enhanced due to the reflected sunlight. Within the clouds layer and in the sub-cloud layer, the photo-dissociation rate depends on the liquid water amount. On the other hand, due to the heterogeneity of the clouds, the perturbed reaction rate coefficients should be studied by spatial patterns rather than slab averaged profile. A first study shows that the NO_2 concentration field below clouds is more vertically distributed and the local difference compared with clear sky case is up to 50%. Apart from the influence on chemistry, the impact of clouds on the dynamics is also important for species vertical profiles. The clouds formation indicates the latent heat release due to liquid water condensation, and the buoyancy produced by this process drives the upwards motion of concentration fields in the cloud layer. Reflected by the shape function, the concentration field is also more vertically distributed.

Turbulent controlled dispersion is a unique aspect in DALES, which is absent in LOTOS-EUROS (Section 3.1.4). The turbulence in this sensitivity study is wind generated. In the boundary layer, the segregation intensity (I_s) are small because the turbulence mixing are efficient. Within the clouds layer, the I_s becomes larger due to the large gradient between the clouds and the environment. The reactants are separately transported because the clouds disrupts the homogeneity of the concentration fields.

After these first tests of model performance, four representative days are chosen to perform realistic simulations over the Rotterdam region, including a winter case at weekend

W1, a winter case at week day W2, a summer case at weekend S1 and a summer case at week day S2. Before the comparison of two models, the simulations are evaluated by the OMI satellite data. The evaluation shows that both model outputs are within the 95% confidence level, indicating the model simulations are reliable.

Ideally, to compare the DALES and LOTOS-EUROS simulation, a relative high resolution is necessary (e.g. 50 $m\times$ 50 $m\times$ 35 m) to resolve the turbulence above this sub-gird. However, such a high resolution simulation is challenging because the computational resources available for this study was not entirely feasible for practical reasons (available resources for data storage and processing), plus the limited capability of personal computer to process the spatial information. As a result, a compromising method is using a coarse resolution (500 $m\times$ 500 $m\times$ 35 m), at the cost of turbulent influence on horizontal variation of concentration field. As presented in Appendix A, the slab averaged quantities under fine and coarse resolution are studied. The comparison shows that the slab averaged concentration profiles are similar between two simulations, and this difference for NO_2 is only 13.22%.

Another consideration is the meteorological inputs. Although LOTOS-EUROS employs ECMWF to drive meteorological development, the ECMWF is less compatible with DALES. For example, the missing of large scale forcing terms, the resolution of data is vary coarse, the availability of surface condition restricts that only constant surface fluxes can be used, etc. All these problems will evolve into unrealistic meteorology. Therefore, in the Rotterdam simulations, the RACMO meteorology is used in this study, with time-dependent surface fluxes and large scale forcing terms. Appendix B, however, shows that the meteorological inputs have limited influence on concentration fields. By comparing the RACMO and ECMWF driven simulations, under the same cases, even the development of dynamics differ considerably, the difference in slab averaged profiles is normally smaller than 10%. From the two additional experiments in Appendix, one can conclude that in terms of slab averaged quantities, the constraint of concentration boundary condition form LOTOS-EUROS overwhelms the effect from dynamics.

In the final part, the consistency between DALES and LOTOS-EUROS is evaluated in terms of vertical, horizontal and temporal patterns. Here lists a conclusive comparison between the two models. But it is important to note that the difference between two models at these aspects are quite depends on the DALES domain size, the larger domain size, the smaller influence of the boundary conditions.

Concentration fields. Slab averaged LOTOS-EUROS concentration at 6 a.m. of local time serve as initial inputs for DALES. With the onset of simulation, LOTOS-EUROS constrains hourly passive scalar boundary condition in DALES. It is the nesting technique that ensures the DALES slab averaged profiles are highly consistent with LOTOS-EUROS. In terms of horizontal spatial patterns, despite the coarse resolution that can not resolve turbulence, the resolution of DALES simulation is still much higher than LOTOS-EUROS that reveals much more information about the spatial variation.

Meteorology. LOTOS-EUROS employs the ECMWF meteorological data at every 3 hour. DALES, instead uses more compatible meteorological inputs, RACMO, with time-dependent

forcing and surface fluxes every 3 hour. Although two models uses difference meteorological inputs, the outputs of profiles are similar to each other. The influence of clouds in DALES, for example, is not reflected by the profiles. The constraint by LOTOS-EUROS overwhelms the meteorological influence on profiles.

Dynamics scheme. The dynamics is a important property that distinct DALES from LOTOS-EUROS. DALES directly solves the turbulence above a certain filter width. But due to the limitation of restore space and processing capability, this property is not considered in Rotterdam simulations.

Chemistry scheme. The chemical mechanism applied in this thesis only consists of NO_x and O_3. Other species such as VOCs are not included. Contrary, the LOTOS-EUROS contains a more completed reactants system. Besides, the chemistry algorithm solver in DALES and LOTOS-EUROS are also different. The chemical scheme cloud be the main reason of the difference in temporal variability.

Emission sources. The heterogeneous emission in DALES is from URBIS traffic emission. After processing, only the NO emission is applied in the simulation. However, the emission inventory employed in LOTOS-EUROS is MACC-III that contains various air pollutant emissions. Both the emission sources apply the same monthly, weekly and diurnal factors. The heterogeneous sources and resolution lead to the considerable difference in horizontal distribution.

The research outputs show that the slab averaged profiles simulated by DALES are highly consistent with LOTOS-EUROS simulations. In terms of NO_2 fraction, for the majority cases the largest difference is in the boundary layer at the beginning of the simulations, where there is considerable discrepancy in the NO profiles. This difference can up to 20%. The profile shape function, on the other hand, does not show significant influence from dynamics. For this DALES domain size the constraint of concentration boundary condition from LOTOS-EUROS overwhelms other influences.

The time series of slab averaged surface concentration ($c(0)$) and vertical integrated column density (N^V) provide the reference to study the spatial variability of concentration fields. Under the majority of the cases, both the model simulations are consistent with each other, especially after 12. p.m.. The main discrepancy is caused by the temporal difference, which may because of the reaction rate coefficients, chemical mechanism, etc. In one of the case (W1), the difference between two models seems to be a systematic bias, the reason cloud be the reaction rate coefficient or chemical mechanism. Generally, the trend of N^V is similar as $C(0)$, and both models are more consistent in terms of N^V, the difference is in range of 13% to 26%.

To further study the spatial patterns of NO_2 concentration distribution, there are 5 stations that sparsely located in the region of interests. Compared with LOTOS-EUROS, DALES shows more spatial variability due to its higher resolution. Among all the cases, the winter case W2 shows the highest representativeness, the overall difference compared with slab averaged values are less than 20%, while the summer case S1 shows the highest spatial variability. The local $c(0)$ difference when compared with the slab averaged depends on the

wind direction, and relative location to high concentration or sources.

4.2 Outlook

An air pollutant dispersion model that based on the computational fluid dynamics tends to be the dominating tool to study the urban scale air quality. This kind of numerical model is of importance to study the vertical distribution of the air pollutants. Hereto, this thesis makes the first step to develop an air quality module based on an existing large eddy simulation (LES) model, Dutch Atmospheric Large Eddy Simulation (DALES), to test the potential benefits cloud be brought by this new dynamic scheme.

In the sensitivity study, the unique atmospheric dynamics patterns in DALES are presented. But in the latter simulations, due to the computational resources limits feasibility to simulate a high resolution simulation, a compromising method by using coarse resolution is applied. Although for slab averaged quantities, decreasing the resolution does not matter so much, the turbulent influence is not involved in comparison with LOTOS-EUROS simulation. In the future research, better computational resources are necessary to study how turbulence influences the distribution of the concentration on local scale.

Meteorological inputs is another challenge. Meteorology influences concentration by two ways. One is perturbing the reaction rate coefficients, of which influence is limited if taking slab averaging. Another is physical transport by evolution of boundary layer or the clouds. No matter using different meteorological driver or simulating on a higher resolution that can resolve the turbulent influence, the difference due to meteorology is not significant. The reason would be the strong constraint from LOTOS-EUROS boundary condition due to this relatively small domain size. The dependency of meteorological influence on domain size is necessary to explore in future.

Apart from the difference in atmospheric dynamics, the emission inventory is an important factor differing DALES from LOTOS-EUROS. In this thesis, only the traffic emission from URBIS is available. Once the MACC-III emission inventory is available, which is employed by LOTOS-EUROS, it is worth to evaluate to what extent the emission inventory affects the concentration fields evolution. Moreover, the chemical mechanism and chemistry solver cloud also be a reason that leads to the discrepancy in concentrations fields. This is not included in this thesis and desired to be study in following research.

The potential benefits of DALES in urban air quality study are revealed in the sensitivity study, but due to the limited computational resources, these patterns are not involved in the comparison with LOTOS-EUROS, a widely used air quality model nowadays. But once the facilities are powerful enough, the dynamics of this state-of-art numerical model will considerably impacts the distribution of concentration fields. With the improvements mentioned above, this air quality module based on DALES cloud be more favorable in urban air quality research.

Bibliography

[WHO et al.(2000)] WHO et al. Air quality guidelines for europe. 2000.

[WHO et al.(2003)] WHO et al. Health aspects of air pollution with particulate matter, ozone and nitrogen dioxide: report on a who working group, bonn, germany 13-15 january 2003. 2003.

[WHO et al.(2014)] WHO et al. Burden of disease from household air pollution for 2012. *WHO, Geneva*, 2014.

[Daly and Zannetti(2007)] Aaron Daly and Paolo Zannetti. Air pollution modeling–an overview. *Ambient air pollution*, 2007.

[Schaap et al.(2005a)] M Schaap et al. Lotos-euros: Documentation. *TNO report*, 2005a.

[van Jaarsveld et al.(2015)] van Jaarsveld et al. The ops-model. 2015.

[Erbrink(1995)] Johannes Jan Erbrink. *Turbulent Diffusion from Tall Stacks: The Use of Advanced Boundary-layer Meteorological Parameters in the Gaussian Dispersion Model" STACKS"*. VU, 1995.

[Heus et al.(2009)] Thijs Heus et al. Dales31 manual. 2009.

[Beirle(2004)] Steffen Beirle. Estimating source strengths and lifetime of nitrogen oxides from satellite data. 2004.

[Atkinson(2000)] Roger Atkinson. Atmospheric chemistry of vocs and no x. *Atmospheric environment*, 34(12):2063–2101, 2000.

[Logan(1985)] Jennifer A Logan. Tropospheric ozone: Seasonal behavior, trends, and anthropogenic influence. *Journal of Geophysical Research: Atmospheres*, 90(D6):10463–10482, 1985.

[Garg(1998)] Vijay K Garg. *Applied computational fluid dynamics*. CRC Press, 1998.

[Burton(2005)] GC Burton. Large eddy simulation of passive-scalar mixing using multifractal subgrid-scale modeling. *Annual Research Briefs*, pages 211–222, 2005.

[Heus et al.(2010)] Thijs Heus et al. Formulation of the dutch atmospheric large-eddy simulation (dales) and overview of its applications. *Geoscientific Model Development*, 3(2): 415–444, 2010. ISSN 1991-959X.

[Schaap et al.(2008)] M Schaap et al. The lotos-euros model: description, validation and latest developments. *International Journal of Environment and Pollution*, 32(2):270–290, 2008. ISSN 0957-4352.

[Schaap et al.(2005b)] M Schaap et al. Lotos-euros: Documentation. *TNO report*, 2005b.

[de Arellano et al.(2011)] Vilà-Guerau de Arellano et al. The role of boundary layer dynamics on the diurnal evolution of isoprene and the hydroxyl radical over tropical forests. *Journal of Geophysical Research: Atmospheres*, 116(D7), 2011.

[Chang et al.(1987)] JS Chang et al. A three dimensional eulerian acid deposition model: Physical concepts and formulation. *Journal of Geophysical Research: Atmospheres*, 92(D12): 14681–14700, 1987. ISSN 2156-2202.

[Schofield(1967)] K Schofield. An evaluation of kinetic rate data for reactions of neutrals of atmospheric interest. *Planetary and Space Science*, 15(4):643–664, 1967.

[de Arellano et al.(2015)] Jordi Vilà-Guerau de Arellano et al. *Atmospheric boundary layer: Integrating air chemistry and land interactions*. Cambridge University Press, 2015.

[Berrisford et al.(2011)] Berrisford et al. Atmospheric conservation properties in era interim. *Quarterly Journal of the Royal Meteorological Society*, 137(659):1381–1399, 2011. ISSN 1477-870X.

[Dee et al.(2011)] DP Dee et al. The era interim reanalysis: Configuration and performance of the data assimilation system. *Quarterly Journal of the Royal Meteorological Society*, 137 (656):553–597, 2011. ISSN 1477-870X.

[Meijgaard et al.(2008)] Van Meijgaard et al. *The KNMI regional atmospheric climate model RACMO version 2.1*. Koninklijk Nederlands Meteorologisch Instituut, 2008.

[Boersma et al.(2011)] KF Boersma et al. An improved tropospheric no 2 column retrieval algorithm for the ozone monitoring instrument. *Atmospheric Measurement Techniques*, 4 (9):1905–1928, 2011.

[Ouwersloot et al.(2011)] HG Ouwersloot et al. On the segregation of chemical species in a clear boundary layer over heterogeneous land surfaces. *Atmospheric chemistry and physics*, 11(20):10681–10704, 2011. ISSN 1680-7316.

[de Arellano et al.(2005)] Vilà-Guerau de Arellano et al. Transport and chemical transformations influenced by shallow cumulus over land. *Atmospheric Chemistry and Physics*, 5(12): 3219–3231, 2005. ISSN 1680-7316.

[Burrows et al.(2011)] John P Burrows et al. *Tropospheric Remote Sensing from Space*. Springer, 2011.

[McNaught et al.(1997)] Alan D McNaught et al. *Compendium of chemical terminology*, volume 1669. Blackwell Science Oxford, 1997.

[Calvert(1990)] Jack George Calvert. Glossary of atmospheric chemistry terms (recommendations 1990). *Pure and applied chemistry*, 62(11):2167–2219, 1990. ISSN 1365-3075.

[Braslavsky(2007)] Silvia E Braslavsky. Glossary of terms used in photochemistry, (iupac recommendations 2006). *Pure and Applied Chemistry*, 79(3):293–465, 2007. ISSN 1365-3075.

[Joseph et al.(1976)] J H Joseph et al. The delta-eddington approximation for radiative flux transfer. *Journal of the Atmospheric Sciences*, 33(12):2452–2459, 1976.

Appendix A

Influence of resolution on DALES slab averaging quantities

As a large eddy simulation, DALES resolves the turbulences that above the scale of sub-grids. The finer resolution suggests more accurate the simulation. Typically, the horizontal resolution for a urban scale simulation is around 50 m. On this resolution, the output of DALES that describes spatial variability (fielddump.nc file) is too large to restore on the server and to process with limited personal computer. One compromising method is to reduce the resolution. Here, a pair of simulations with coarse and fine resolution is used to prove that in terms of slab averaging quantities, the influence of resolution is limited.

The setting for the simulation can refer to Table. B.1 and Figure. 3.22 and 3.23 in Section 3.2. The comparison is shown in Figure. A.1. The slab averaged profiles of different resolutions are quite similar, except for the ground level concentration, where the difference is considerable. The relative difference between coarse and fine resolution, as shown in Figure. A.2, is almost constant with height. Only near the surface, the discrepancy is significant.The time and height averaged relative difference of NO_2, NO and O_3 are only 13.22%, 26.79% and 18.43% respectively.

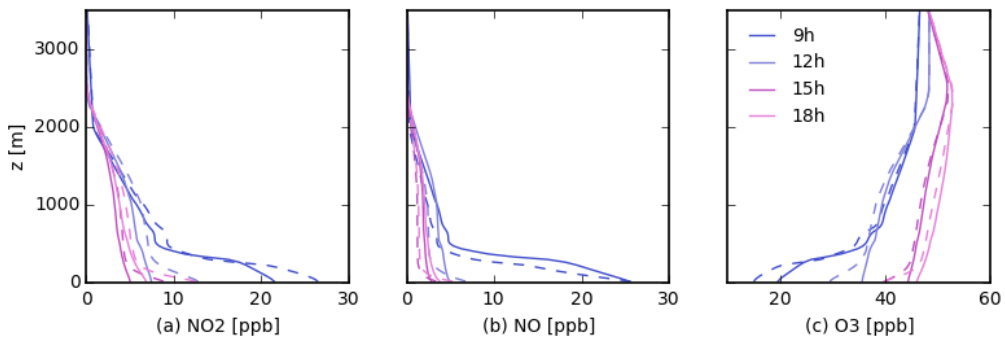

Figure A.1: Evolution of 10-minute slab averaged concentration field of coarse resolution (continuous line) and fine resolution (dashed line) for case S2. (a) NO_2 concentration; (b) NO concentration; (c) O_3 concentration.

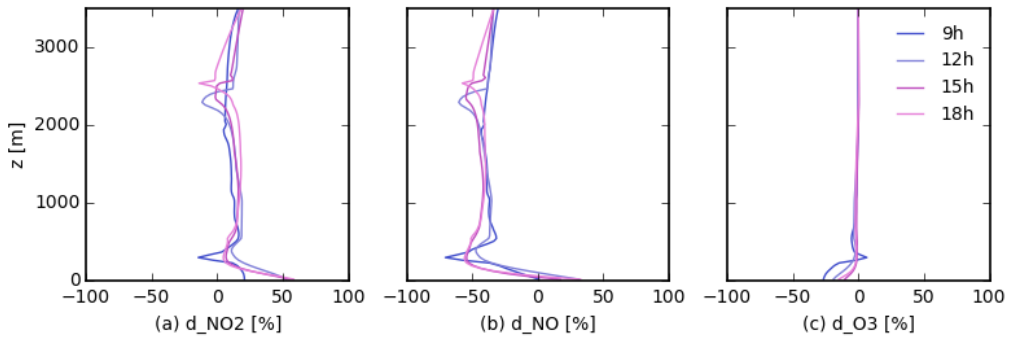

Figure A.2: Evolution of 10-minute slab averaged difference of concentration field between coarse resolution and fine resolution for case S2. (a) NO_2 concentration; (b) NO concentration; (c) O_3 concentration.

Appendix **B**

Influence of meteorology on DALES concentration fields

As presented in Section 3.2, the RACMO driven meteorology fields evolution differ from observations. Principally, to be comparable to LOTOS-EUROS, the simulations with DALES should apply the same meteorology as much as possible. However, compared with RACMO, ECMWF is less compatible to DALES meteorological field. The ECMWF meteorology data can only covers the majority of parameters in DALES with very coarse temporal and spatial resolution. Hereto, in this chapter, two sets of simulation are performed, driven by RACMO and ECMWF meteorology, respectively, in order to study the meteorological influence on concentration fields.

The initial condition of RACMO can refer to Table. B.1, Figure. B.1 and 3.23 in Section 3.2. The parameters from ECMWF are presented in Table. B.1 and Figure. B.1. For ECMWF, no time dependent surface fluxes and large scale forcing terms applied. Both sets of the simulation applies the same concentration fields and boundary conditions.

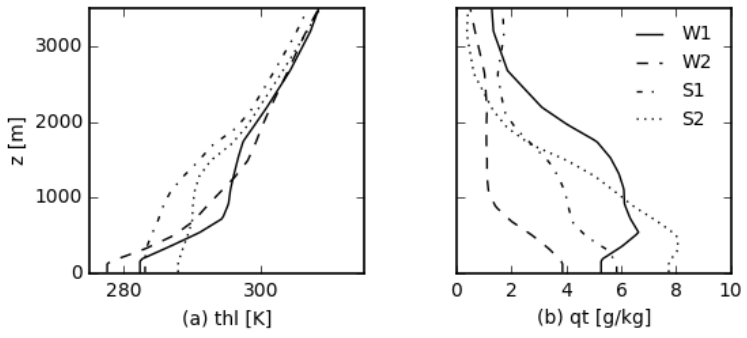

Figure B.1: Initial profiles of RACMO for four cases over Rotterdam region of (a) liquid water potential temperature (θ_l); (b) total water specific humidity (q_t).

The evolution of dynamics are presented from Figure. B.2 to B.5. The difference is considerable. Due to the time dependent surface heat flux, the boundary layer develops deeper in the RACMO. Besides, the none of the cases evolves liquid water content in ECMWF

Table B.1: Parameters in DALES for each case, consisting of a winter case at weekend W1, a winter case in week day W2, a summer case at weekend S1 and a summer case in week day S2. The reaction rate coefficients are referred to [1] [Schaap et al.(2005a)].

Parameter	Unit	W1	W2	S1	S2
Date	-	20111112 (SAT)	20111116 (WED)	20120602 (SAT)	20120626 (TUE)
xday	-	316	320	154	178
xtime	[h]	5	5	4	4
thls	$[K]$	277.619	273.337	283.258	286.198
ps	$[Pa]$	102592.4	102043.3	101799.1	102080.0
$\overline{w'\theta'}$	$[Kms^{-1}]$	0.0270	0.0264	-0.0004	0.0023
$\overline{w'q'}$	$[gkg^{-1}ms^{-1}]$	-0.0018	-0.0013	-0.0031	-0.0029
runtime	$[s]$	43200			
itot	-	40 (400)			
jtot	-	30 (500)			
xsize	$[m]$	20000			
ysize	$[m]$	15000			
kmax	-	100			
xlat	$[\circ]$	51.91			
xlon	$[\circ]$	4.48			
j	$[s^{-1}]$	$1.45 \times 10^{-2} \times e^{\frac{-0.54}{\cos(SZA)}}$[1]			
k	$[cm^3 molec^{-1} s^{-1}]$	$2.00 \times 10^{-12} \times e^{\frac{-1400}{T}}$[1]			
lcloudKconst	-	false			

based simulation. These are due to the simulation only uses fixed surface heat and moisture flux at 6 a.m. of local time, which are not strong enough to develop deep boundary layer and clouds.

The concentration fields responses to meteorology are shown in Figure. B.6 to B.9. Meteorological influence on concentration includes that directly affecting chemical reactions, for example, temperature, radiation, moisture, clouds perturbation on reaction rate coefficients

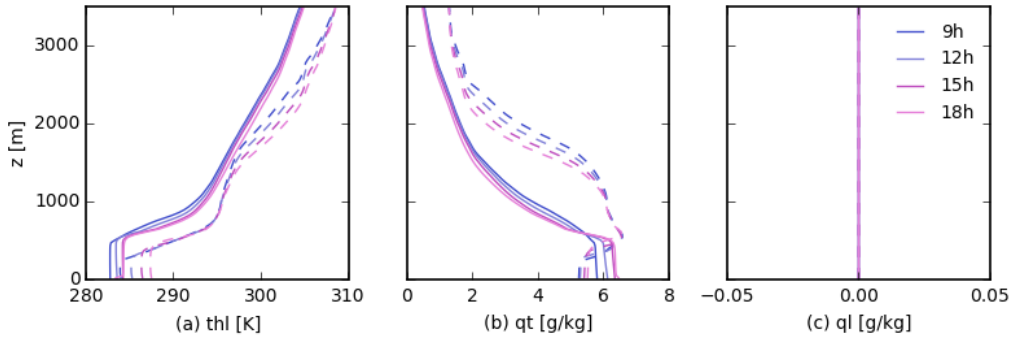

Figure B.2: Evolution of 10-minute slab averaged concentration field profile of RACMO (continuous line) and ECMWF (dashed line) inputs for case W1. (a) NO_2 concentration; (b) NO concentration; (c) O_3 concentration.

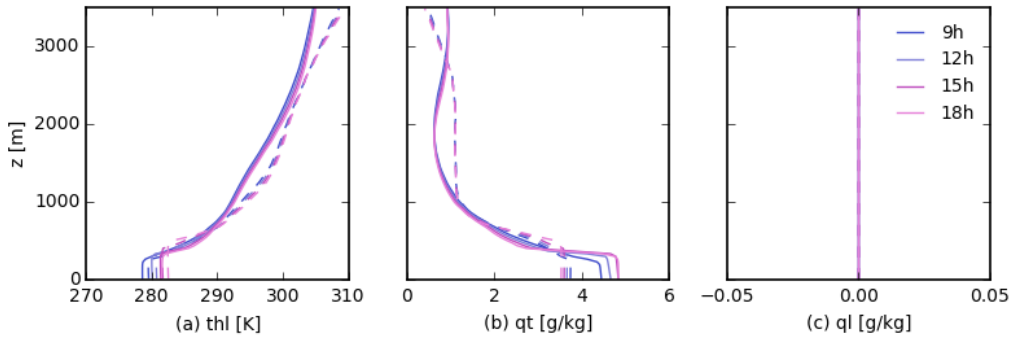

Figure B.3: Evolution of 10-minute slab averaged concentration field profile of RACMO (continuous line) and ECMWF (dashed line) inputs for case W2. (a) NO_2 concentration; (b) NO concentration; (c) O_3 concentration.

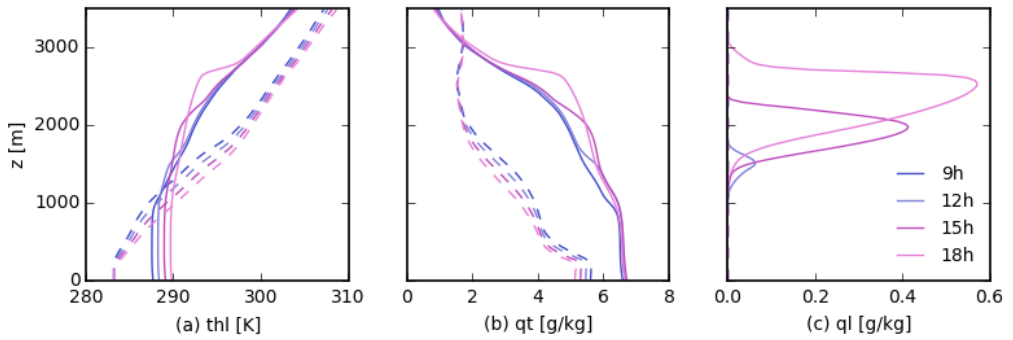

Figure B.4: Evolution of 10-minute slab averaged concentration field profile of RACMO (continuous line) and ECMWF (dashed line) inputs for case S1. (a) NO_2 concentration; (b) NO concentration; (c) O_3 concentration.

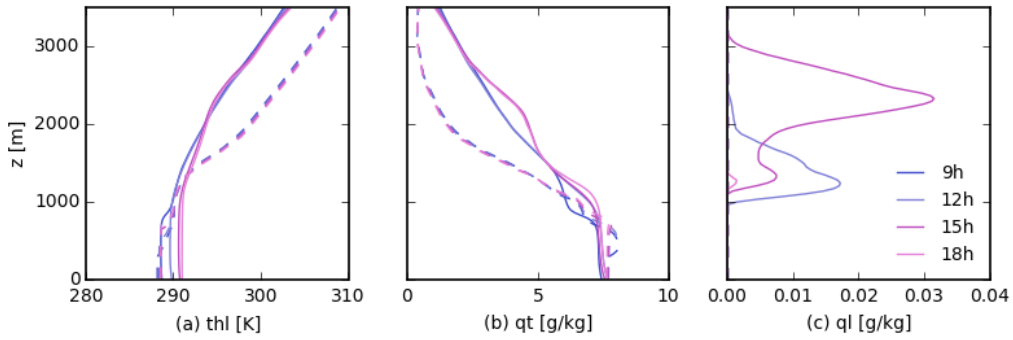

Figure B.5: Evolution of 10-minute slab averaged concentration field profile of RACMO (continuous line) and ECMWF (dashed line) inputs for case S2. (a) NO_2 concentration; (b) NO concentration; (c) O_3 concentration.

and turbulence mixing. These influence is very limited at least for slab averaged profiles, because the correction for reaction rate is very small under the same case; or the redistribution of concentration fields such as the vertical transport by the clouds, and the boundary layer growth that entrains air from free troposphere or dilutes the species in the boundary layer.

Despite of the much deeper boundary layer and the clouds formation in RACMO based simulations, the concentration profiles are still similar to ECMWF driven simulations. The influence of the growing boundary layer and clouds transport are not reflected by profiles. The most significant difference is at the beginning of the simulation. Quantitatively, the averaged relative difference for different species and cases, as shown in Table. B.2, are mainly smaller than 10%. Thus, the inconsistency in meteorology does not lead to large discrepancy in profiles. The high similarity in concentrations attributes to the boundary constraint of LOTOS-EUROS.

Table B.2: Temporal and spatial averaging of relative difference between RACMO and ECMWF for each reactant and case [%].

Reactants	W1	W2	S1	S2
NO_2	8.09	1.34	15.09	8.00
NO	9.35	1.96	24.48	9.85
O_3	6.84	1.65	16.66	6.97

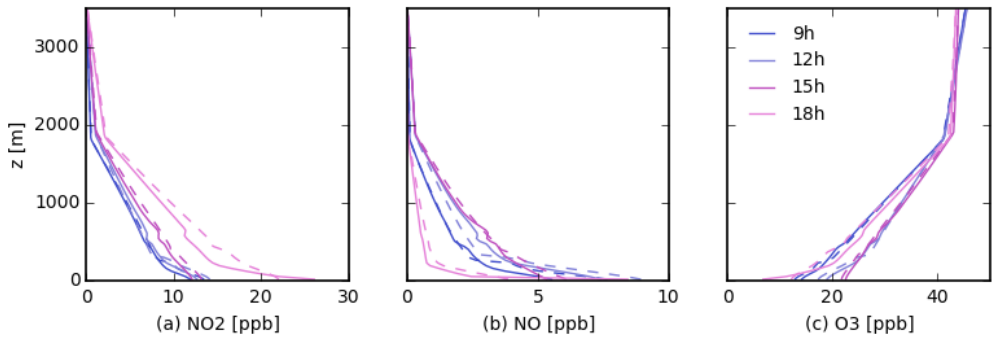

Figure B.6: Evolution of 10-minute slab averaged concentration field profile of RACMO (continuous line) and ECMWF (dashed line) inputs for case W1. (a) NO_2 concentration; (b) NO concentration; (c) O_3 concentration.

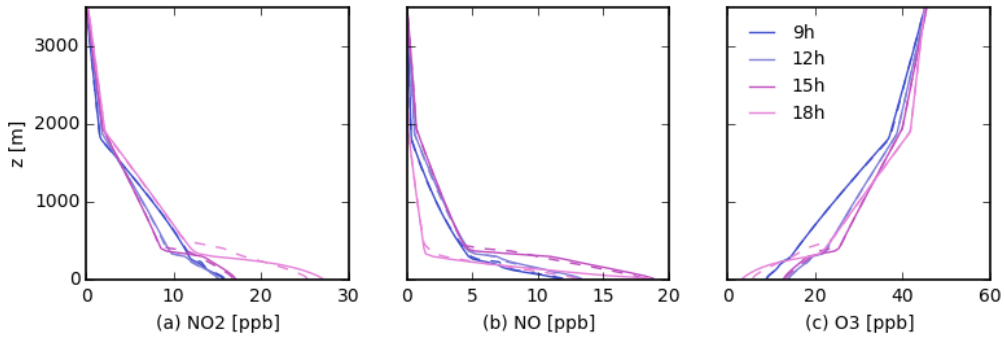

Figure B.7: Evolution of 10-minute slab averaged concentration field profile of RACMO (continuous line) and ECMWF (dashed line) inputs for case W2. (a) NO_2 concentration; (b) NO concentration; (c) O_3 concentration.

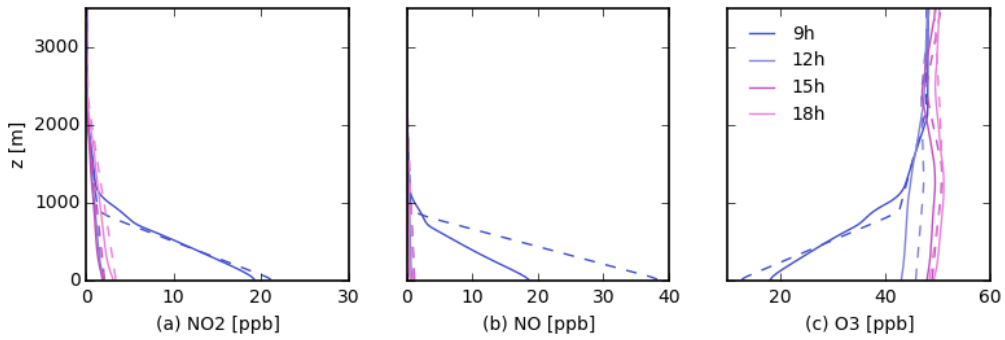

Figure B.8: Evolution of 10-minute slab averaged concentration field profile of RACMO (continuous line) and ECMWF (dashed line) inputs for case S1. (a) NO_2 concentration; (b) NO concentration; (c) O_3 concentration.

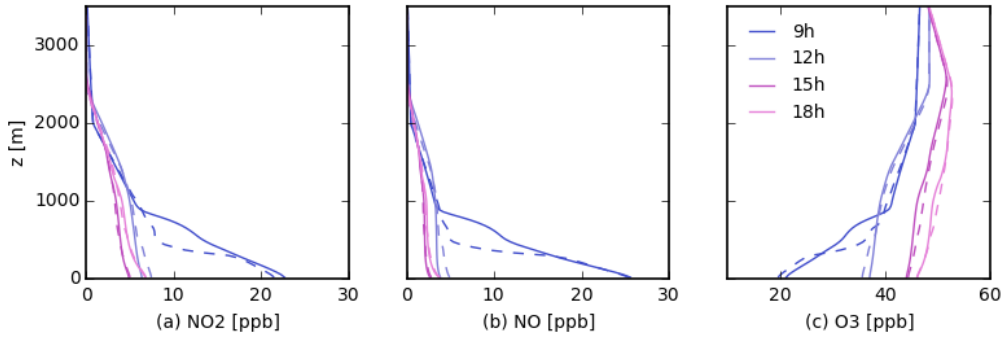

Figure B.9: Evolution of 10-minute slab averaged concentration field profile of RACMO (continuous line) and ECMWF (dashed line) inputs for case S2. (a) NO_2 concentration; (b) NO concentration; (c) O_3 concentration.

Appendix C

Relevant concepts

C.1 Chemical reaction rate

Rate law and orders of reaction is an empirical differential rate equation that of reaction rate and its dependency on concentrations of the reactants [McNaught et al.(1997)]. For two reactants A and B,

$$v = f\Big([A],[B]\Big) = k[A]^m[B]^n \tag{C.1}$$

, where $[\cdot]$ means molar concentration of one species; m and n are partial order of reaction that are independent of concentration and time, and their summation is called total order of the reaction; k is the rate coefficient. The unit of reaction rate is concentration per unit time.

In the first order reaction, the reaction rate is proportional to the concentration of one of the reactants. While the second order reaction means the reaction rate is proportional to square of one specific reactant or product of two different reactants, and so on.

By integration, the concentration changes with time for the first order reaction can be re-written as so-called exponential decay,

$$\frac{d[A]}{dt} = -k[A] \tag{C.2a}$$

$$[A] = [A]_0 e^{-kt} \tag{C.2b}$$

, where $[A]_0$ is the initial concentration of A. For a simple second order reactions,

$$\frac{d[A]}{dt} = -k[A]^2 \tag{C.3a}$$

$$\frac{1}{[A]} = \frac{1}{[A]_0} + kt \tag{C.3b}$$

$$\tag{C.3c}$$

For a mixed second order reactions,

$$\frac{d[A]}{dt} = -k[A][B] \tag{C.4a}$$

$$\frac{[A]}{[B]} = \frac{[A]_0}{[B]_0} e^{([A]_0 - [B]_0)kt} \tag{C.4b}$$

Pseudo first order reactions happens in a second order reaction, where the concentration of one of the reactants exceeds others during chemical mixture [McNaught et al.(1997)]. For example, if $[A]_0 << [B]_0$, under which reactant B can be assumed to be constant during mixture. The reaction rate for reactant A is,

$$\frac{d[A]}{dt} = -k[A][B]_0 \tag{C.5a}$$

$$\frac{d[A]}{dt} = -k_{obs}[A] \tag{C.5b}$$

, where the k_{obs} is observed rate constant, and referred to a pseudo first order rate coefficient. The pseudo first order reactions is a solution widely used when measuring a second order reaction rate becomes problematic.

Rate coefficient quantifies the rate of reactions, which is only determined experimentally. Except for elementary reactions, which can be calculated by molecular dynamics simulation. For a reversible bimolecular elementary process, the second order rate law is applied. Reaction rate constant is commonly dependent on temperature, total pressure, etc [Calvert(1990)]. The rate coefficient is of dimension of concentration^{1-p} per unit time, where p is the number of reactants.

Elementary reaction is a single step reaction with a single transition state without intermediates detected, or needed to be postulated in order to describe the chemical reaction on a molecular scale [McNaught et al.(1997)].

Reaction mechanism describes the process as complete as possible, which must consist of the reaction stoichiometry, the rate law and with all other available experimental data.

Lifetime for a first-order kinetics decaying entity, is the time needed for a concentration of the entity to decrease exponentially from its initial value. It is mathematically defined as follows,

$$\tau = \frac{1}{k} = \frac{1}{\sum_i k_i} \tag{C.6}$$

, where k_i the first-order rate constants for all processes causing the decay of the molecular entity. For non-first order processes, the lifetime depends on the initial concentration of the entity. In this case, an initial or average lifetime is defined, which is called decay time [Calvert(1990)] [McNaught et al.(1997)].

C.2 Photochemistry

Photochemistry describes a chemical reaction caused by absorption of ultraviolet (UV), visible or infrared radiation [McNaught et al.(1997)].

Photolysis is bond cleavage due to UV, visible or infrared radiation [Braslavsky(2007)].

j-values is an effective first order rate coefficient for photochemical reaction of light-absorbing impurities [Calvert(1990)]. For example, a chemical species X is photo-decomposed into A and B,

$$X + h\upsilon \rightarrow A + B \tag{C.7a}$$

$$j = \int \sigma(\lambda)\phi(\lambda)S(\lambda)d\lambda \tag{C.7b}$$

, where $\sigma(\lambda)$ is the absorption cross section of X at wavelength λ; $\phi(\lambda)$ is the primary quantum yield; $S(\lambda)$ is the actinic flux.

Actinic flux is the quantity of light available to molecules at a particular point in the atmosphere, which drives photochemical processes due to absorption and scattering [Calvert(1990)].

$$S(\lambda) = \int_{\theta}\int_{\phi} \frac{L(\lambda,\theta,\phi)}{\left(\frac{hc}{\lambda}\right)} \sin\theta d\theta d\phi \tag{C.8}$$

, where $L(\lambda,\theta,\phi)$ is the spectral radiance over all directions at wavelength λ; θ and ϕ are the zenith angle and azimuth angle respectively;hc/λ is the energy per quantum of light wavelength. The unit is [$quantacm^{-2}s^{-1}nm^{-1}$].

Leighton relationship describes the tropospheric ozone produced by nitrogen oxides.

$$[O_3] = \frac{j[NO_2]}{k[NO]} \tag{C.9}$$

, where [$\cdot$] means concentration; j is the photolysis rate and k is the second order reaction rate.

C.3 Other concepts

Friction velocity is the shear stress in form of velocity, also called shear velocity. It describes the diffusion and dispersion of particles in the fluids,

$$U_* = \sqrt{\frac{\tau}{\rho}} \tag{C.10}$$

, where τ is the shear stress and rho is the density of the fluid.

Monin-Obukhov length is the height where the turbulence is generated more by turbulence than wind shear,

$$L = -\frac{U_*^3 \overline{\theta_v}}{kg(\overline{w'\theta'_v})_s} \tag{C.11}$$

, where U_* is the friction velocity; $\overline{\theta_v}$ is the virtual temperature; k is the Karman constant; g is the gravitational acceleration and $(\overline{w'theta'_v})_s$ is the surface virtual temperature flux.

Solar zenith angle (SZA) is the angle between zenith and the center of the Sun disc.

$$\cos\chi_0 = \sin\phi\sin\delta + \cos\phi cos\delta\cos h \tag{C.12}$$

, where χ_0 is the SZA, ϕ is the local latitude, δ is the current declination of the Sun, and h is the hour angle in local hour time.

Cloud optical depth is the total vertical extinction of light by scattering and absorption due to clouds.

$$\tau_c = \frac{3}{2}\frac{LWP(z')}{\rho_w r_e} \tag{C.13}$$

, with LWP is the liquid water path ([kgm^{-2}], Equation.C.15), and r_e is the effective radius of the cloud ([m], Equation. C.16).

Transmission coefficient describes the effectiveness of light passes through a surface or an optical element. It can be derived numerically from delta-Eddington theory [Joseph et al.(1976)],

$$tr = \frac{\tau_{c0} - e^{-\tau_c}}{4 + 3\cdot\tau_c\cdot(1-f)} \tag{C.14}$$

, where τ_c is the cloud optical depth; f is the scattering phase function asymmetry factor, which equals to 0.86 for the typical cloud particle size ranges.

Liquid water path is the total amount of liquid water present between a certain height z' and the top of the atmosphere ([kgm^{-2}]).

$$LWP(z') = \int_{z'}^{\infty} q_{l0}(z')dz' \tag{C.15}$$

, where $q_{l0}(z')$ is the liquid water content at z'.

Cloud drop effective radius is a weighted mean of the size distribution of cloud droplets.

$$r_e(z) = \frac{\int_0^\infty n(r,z)r^3 dr}{\int_0^\infty n(r,z)r^2 dr} \tag{C.16}$$

, where $n(r,z)$ is the size distribution function of could droplets, the default value in DALES is $10\mu m$.

Slant column density (SCD) is the volume number concentration profile for a certain trace gas along the slant photon path [Burrows et al.(2011)],

$$N^S = \int_0^{TOA} c(z)m(z)dz \tag{C.17}$$

, where z is the altitude ($[m]$), TOA is the top of the atmosphere, $c(z)$ is the concentration as function of height ($[moleculesm^{-3}]$) and $m(z)$ is the height dependent air mass factor. SCD is the amount that directly measured by instrument.

Vertical column density (N^V) is the total amount of molecules in a vertical column of the atmosphere [Burrows et al.(2011)],

$$N^V = \int_0^{TOA} c(z)dz \tag{C.18}$$

, where z is the altitude ($[m]$), TOA is the top of the atmosphere, and $c(z)$ is the concentration as function of height ($[moleculesm^{-3}]$). Unlike slant column density (SCD), N^V is independent to measurement techniques, viewing direction and wavelength, but only refers to atmosphere itself.

Air mass factor (AMF) is the ratio between slant column density (N^S) and vertical column density (N_V),

$$M = \frac{N^S}{N^V} \tag{C.19}$$

The AMF can be assumes same for all photons in case of direct sun observation, and can be calculated geometrically [Burrows et al.(2011)],

$$M = \frac{1}{\cos(\mu_0)} \tag{C.20}$$

,where μ_0 is the SZA. While in case of scattered light, the air mass AMF is determined by a radiative transfer model (RTM).

Height dependent air mass factor (box AMF or block AMF) is a height-resolved partial air mass factor for specific atmospheric layers in order to quantify the vertical dependence of the measurement sensitivity. For observations of trace gases at visible or UV wavelengths, due to Rayleigh scattering on air molecules, the light paths could be very complex. As a result, the air mass factor of each atmospheric layer is no more simply determined by geometric considerations. Instead, a numerical radiative transfer simulations have to simulate the air mass factor, such as DISAMAR [Burrows et al.(2011)],

$$M_i = \frac{N_i^S}{N_i^V} \tag{C.21}$$

, where N^S and N^V are slant column density and vertical column density, the subscribe i indicates the specific atmospheric layer.

C.4 Unit conversion

Mass concentration is the mass of i divided by the volume of the atmosphere V, and normally of unit [gcm^{-3}] or [μgcm^{-3}],

$$\rho_i = \frac{m_i}{V} \tag{C.22}$$

Number concentration is the number of molecules in the atmosphere of volume V.

$$c_i = \frac{N_i}{V} \tag{C.23a}$$

$$N_i = \frac{m_i}{M_i} N_A \tag{C.23b}$$

, where N_i is the number of molecules for species i, the M_i is molar mass ([$gmol^{-1}$]), and N_A is Avogadro constant ($6.023 \times 10^{23} mol^{-1}$).

Mixing ratio is defined as the ratio of the number concentration of the species i to that of the atmosphere.

$$r_i = \frac{n_i}{n_{tot}} = \frac{m_i}{m_{tot}} \tag{C.24a}$$

$$n_i = \frac{N_i}{N_A} = \frac{m_i}{M_i} \tag{C.24b}$$

$$\tag{C.24c}$$

, where n_{tot} and n_i are the amount of substance of the mixture and species i, respectively ([mol]); m_{tot} and m_i are the mass of the mixture and species i.